Alma Mater Studiorum · University of Bologna

School of Science
Department of Physics and Astronomy
Master Degree in Physics

Image Enhancement for a Bose-Einstein Condensate Interferometer

Supervisor:
Dr. Francesco Minardi

Submitted by:
Luca Cavicchioli

Academic Year 2019/2020

Sommario

L’atomo, grazie al suo comportamento ondulatorio, può manifestare fenomeni associati, nell’esperienza comune, alla luce: l’interferenza è uno di questi. La possibilità di raffreddare nubi atomiche e di manipolare gli stati degli atomi ivi situati ha aperto molte nuove opportunità per sfruttare questi stati per svariati utilizzi, uno dei quali è la misura di vari tipi di osservabili fisiche con altissima precisione, grazie ai succitati fenomeni di interferenza: l’interferometria atomica.

Sin da quando sono stati ottenuti i primi condensati di Bose-Einstein in gas atomici, l’interferenza tra di essi ha suscitato un vivo interesse, in quanto si tratterebbe di osservare direttamente fenomeni di coerenza quantistica tra oggetti di dimensioni macroscopiche. Tuttavia, a differenza delle nubi atomiche *termiche*, per i condensati l’alta densità atomica rende difficile ignorare gli effetti delle interazioni all’interno degli stessi. Per le applicazioni, è di fondamentale importanza comprendere il ruolo delle interazioni nella formazione delle figure d’interferenza.

In questa tesi è stato sviluppato un algoritmo per migliorare la qualità delle immagini in assorbimento di un condensato. Questo algoritmo calcola una base di immagini per il rumore e rimuove la proiezione dell’immagine di partenza da questa base, ottenendo così un’immagine contenente, idealmente, solo il segnale. È stato poi utilizzato per la pulizia di immagini ottenute da interferometria atomica. Queste immagini sono state analizzate utilizzando due tecniche, e i risultati ottenuti sono stati comparati a quelli per il caso di un condensato ideale. I risultati trovati sono incompatibili con il caso ideale, e sono quindi frutto delle interazioni tra atomi.

Abstract

The atom, thanks to its wave behaviour, can manifest phenomena which are, usually, associated to light: interference is one of them. The possibility of cooling atomic clouds and manipulating the states of the atoms contained in them opened many new opportunities to exploit these states in many ways; one of them is measuring various kinds of physical observables with high precision, thanks to the aforementioned interference phenomena: this is atom interferometry.

Since the first Bose-Einstein condensates in atomic gases were obtained, there has been a keen interest in interference between them, as it would mean to observe coherent quantum phenomena between macroscopic objects. Nevertheless, the high atomic density of condensates with respect to non condensed, *thermal*, atomic clouds makes it difficult to ignore the effects of interactions within them. For the applications, understanding the role of interactions in the formation of interference figures is crucial.

In this thesis, an algorithm for the enhancement of absorption images of a condensate has been developed. This algorithm computes an image basis for the noise and then remove the projection of the starting image from this basis, thus obtaining a clean image. This algorithm has then been applied to the enhancement of images obtained from atom interferometry. These images have then been analyzed using two techniques, and the obtained results have been compared to those for an ideal condensate. The results have been found not compatible with the ideal case, and are then due to atom-atom interactions.

Contents

Introduction

This thesis concerns the development of an image-enhancing algorithm used for cleaning absorption images of Bose-Einstein condensates, for its usage in the K-Rb experiment at *LENS (Laboratorio Europeo di Spettroscopia Non lineare)*, and the application of this algorithm to remove noise from interferometric images created in that same experiment.

In the first chapter, we detail the theoretical framework that is used in this kind of experiment. We first start with a brief treatment of atom-light interaction and of the diffraction of atoms by light gratings, both thin and thick, that are used in an atom interferometer as beam splitters. Then, the principal result of the theory of Bose-Einstein condensates, in the ideal and weakly interacting case. In the next section, we explain the origins of the phase shifts, and how these can be used, with atom interferometry, to measure external fields. Finally, the last section concerns how all these pieces come together to enable the creation of an atom interferometer.

The second chapter reports the development of the denoising algorithm that is the subject of this thesis. First, some background and theoretical motivation behind this algorithm and absorption imaging is given, then all the steps of the algorithm are explained in detail. In the next sections, we report what optimizations we have considered, how the test images have been obtained, and the results of the optimization tests. In the last section, the overall performance of the optimized algorithm is assessed in two different variants.

In the third chapter, we apply the algorithm to the denoising of interferometric images and analyze them. First, the experimental procedure used to obtain the images is explained. Then, in the next sections, two techniques of analysis are used to extract the wavenumber of the interference fringes; the expected wavenumber is calculated for an ideal Bose gas, and finally the experimental wavenumbers are compared to the theoretical prediction.

In the last chapter, the conclusions both concerning the developed algorithm

and the fringe formation are given, along with some future prospects for the work started in this thesis.

1

Theoretical setting

Atomic interferometry relies crucially on some of the most peculiar features of quantum mechanics, that is, the wave-particle duality and the superposition of states. Nevertheless, the steps needed for an interferometry experiment are few and with a direct optical analogue. First, the incoming beam has to be split in two paths, that will then have a different evolution and therefore a different phase; these two waves then will be recombined, and will produce interference fringes.

In this chapter we shall review some important results in order to understand the theory behind atomic interferometry with Bose-Einstein condensates. In section 1.1 we will see how the mechanism of interaction of light with atoms can be exploited to create a beam splitter for atoms. In section 1.2 we explain how to obtain a simple model for the evolution of the wave function of a BEC. The evolution of the phase in the two arms of the interferometer is detailed in section 1.3, and then in section 1.4 we will have a look at how these pieces come together.

1.1 Atom-light diffraction

The core mechanism of matter-wave interferometry is coherent scattering, that makes possible the manipulation of particles with the aim of obtaining interference. For the case of atoms, experiments have been made using a wide variety of methods for achieving such a splitting, that can be divided in the two main families of mechanical methods and light methods. In the following pages, only the latter will be treated, and only in two main cases; an exhaustive review of atom interferometry methods is given in [1]. To understand light beam-splitters, we preliminarily introduce a simple model of the atom-light interaction.

1.1.1 Semiclassical atom-light interaction

One of the most used models for the problem of atom-light interaction is the so called *semiclassical model*, in which the radiation field is treated classically, while the atom is quantized. In this subsection, we will briefly recall the main results for this model, following the analysis in [2, P. 151 and following].

In its most straightforward implementation, the atom is treated as a two level system with the states $|g\rangle$ and $|e\rangle$, respectively called the ground and excited states, separated by an energy gap $E_e - E_g = \hbar\omega_{eg}$; the classical field, on the other hand, is a monochromatic and completely polarized field, i.e. the field obtained with an ideal laser:

$$\begin{aligned} \boldsymbol{E}(t) &= \boldsymbol{\epsilon}\frac{E_0}{2}\cos(\omega_L t) \\ &= \boldsymbol{E}_0^{(+)}e^{-i\omega_L t} + \boldsymbol{E}_0^{(-)}e^{i\omega_L t} \end{aligned} \tag{1.1}$$

where $\boldsymbol{\epsilon}$ is the polarization vector and ω_L is the frequency of the wave. Following [2], we split the field in a co-rotating component $\boldsymbol{E}^{(+)}$ and a counter-rotating component $\boldsymbol{E}^{(-)}$.

Our transitions of interest are in the optical regime, and have a radiation wavelength in the range 300 nm–800 nm; this is much larger than the size of an atom, and we are thus justified in approximating the atom as a dipole. Making also the assumption of a single electron[1], we can write the interaction Hamiltonian as

$$\mathscr{H}_{\text{int}} = -e\underbrace{\hat{\boldsymbol{r}}}_{\hat{\boldsymbol{d}}}\cdot\boldsymbol{E}, \tag{1.2}$$

where $-e$ is the charge of the electron. Note that the position operator $\boldsymbol{r}$ is, under parity, odd: as the atomic Hamiltonian is parity invariant, its eigenstates can be chosen from those with well-defined parity, hence the interaction Hamiltonian

---

[1] For the majority of experiments made with quantum gases alkali atoms are used, so this assumption is generally justified.

only has off-diagonal components. We can separate the components of the dipole operator like in Eq. (1.1):

$$\hat{\boldsymbol{d}} = \langle e|\hat{\boldsymbol{d}}|g\rangle |e\rangle\langle g| + h.c. = \hat{\boldsymbol{d}}^{(+)} + \hat{\boldsymbol{d}}^{(-)}$$

and so we see that $\hat{\boldsymbol{d}}^{(\pm)}$ evolves in time with the frequency $\mp\omega_{eg}$. If we carry out the multiplication $\hat{\boldsymbol{d}}\cdot\hat{\boldsymbol{E}}$, the product of the two co-rotating components and that of the two counter-rotating components will evolve with an angular frequency of $\mp(\omega_L + \omega_{eg})$, respectively, while the cross terms will evolve with an angular frequency $\mp(\omega_L - \omega_{eg}) = \mp\Delta$. In the limit $\Delta \to 0$, we can retain only the two cross terms, as the direct terms will be averaged out: this approximation is called the *Rotating Wave Approximation*.

The complete Hamiltonian then is

$$\mathcal{H} = \hbar\omega_{eg}|e\rangle\langle e| - \frac{\hbar\Omega}{2}\left(e^{-i\omega_L t}|e\rangle\langle g| + e^{i\omega_L t}|g\rangle\langle e|\right),$$

where

$$\Omega = \frac{\langle g|\boldsymbol{\epsilon}\cdot\hat{\boldsymbol{d}}|e\rangle}{\hbar}E_0$$

is called the *Rabi frequency*. We can write the Schrödinger equation for the state $|\Psi\rangle = \alpha(t)|g\rangle + \beta(t)|e\rangle$:

$$\begin{cases} \dfrac{\partial}{\partial t}\alpha = i\dfrac{\Omega}{2}\beta e^{i\omega_L t} \\ \dfrac{\partial}{\partial t}\beta = -i\omega_{ge}\beta + i\dfrac{\Omega}{2}\alpha e^{-i\omega_L t}, \end{cases}$$

that we can solve by doing the transformation $\tilde{\beta} = \beta e^{i\omega_L t}$, that results in

$$\begin{cases} \dfrac{\partial}{\partial t}\alpha = i\dfrac{\Omega}{2}\tilde{\beta} \\ \dfrac{\partial}{\partial t}\tilde{\beta} = -i\Delta\tilde{\beta} + i\dfrac{\Omega}{2}\alpha. \end{cases}$$

Those equations can be solved by doing a partial derivative with respect to t and eliminating the variables that appear in both equations.

The general result is

$$\begin{cases} \alpha(t) = e^{i\frac{\Delta}{2}t}\left(\alpha(0)\cos\left(\dfrac{\tilde{\Omega}}{2}t\right) - \dfrac{i}{\tilde{\Omega}}\left(\Delta\alpha(0) + \Omega\tilde{\beta}(0)\right)\sin\left(\dfrac{\tilde{\Omega}}{2}t\right)\right) \\ \tilde{\beta}(t) = e^{i\frac{\Delta}{2}t}\left(\tilde{\beta}(0)\cos\left(\dfrac{\tilde{\Omega}}{2}t\right) - \dfrac{i}{\tilde{\Omega}}\left(\Delta\tilde{\beta}(0) - \Omega\alpha(0)\right)\sin\left(\dfrac{\tilde{\Omega}}{2}t\right)\right), \end{cases} \tag{1.3}$$

where $\tilde{\Omega} = \sqrt{\Omega^2 + \Delta^2}$ is the *generalized Rabi frequency*. For the special case of peculiar interest for which the atoms are initially all in the $|g\rangle$ state, i.e. $\alpha(0) = 1$ and $\tilde{\beta}(0) = 0$ in (1.3), we have that the probability for the atom to be in the excited state is

$$\tilde{\beta}^2(t) = \left(\frac{\Omega}{\tilde{\Omega}}\right)^2 \sin^2\left(\frac{\tilde{\Omega}}{2}t\right), \tag{1.4}$$

This phenomenon of the oscillation of the probability of being in the excited state with time is called *Rabi flopping* or *Rabi oscillation*. When talking about light pulses, one usually refers to the quantity $\tilde{\Omega}\tau$ in the sine of Eq. (1.4) as an angle: for example, a $\pi/2$ pulse is one for which $\tilde{\beta}^2 \propto \sin^2(\pi/4) = 1/2$; in the resonant case, for which $\tilde{\Omega} = \Omega$, this pulse puts the wave function in an equal superposition of $|e\rangle$ and $|g\rangle$.

1.1.2 General theory of the atom beam splitter

We have now the basic results needed to understand the physics of an atomic beam splitter made with an electromagnetic field. The first step in the theory of the atom beam splitter is to have a model of the interaction of an atom with a travelling wave, taking also in consideration the motion of the centre of mass of the atom, and then to superpose two travelling waves in order to understand the scattering of an atom by a light grating. We will follow for this endeavour the treatment in [3] and [4] , respectively. Another point of view, using Bloch states that propagate in a light grating, is detailed in [5].

An atom, initially in the internal ground state and with a centre-of-mass momentum $\boldsymbol{p}$, i.e. in the state $|g, \mathrm{p}\rangle$, traverses a laser beam of frequency ω_L and wavenumber k_L, as sketched in figure 1.1. In the interacting Hamiltonian (1.2) we can write

$$\boldsymbol{E}_0(x,z) = \boldsymbol{\epsilon} E_0(x) e^{ik_L z}.$$

The field will affect appreciably only the z component of the atomic momentum: this means that, for a state $|p_z\rangle$

$$e^{ik_L z}|p_z\rangle = |p_z + \hbar k_L\rangle,$$

and there is a coupling between the state $|g, p_z\rangle$ and the state $|e, p_z + \hbar k_L\rangle$; we will denote $|p_z \pm n\hbar k_L\rangle$ as $|\pm n\rangle$. Another consequence of this approximation

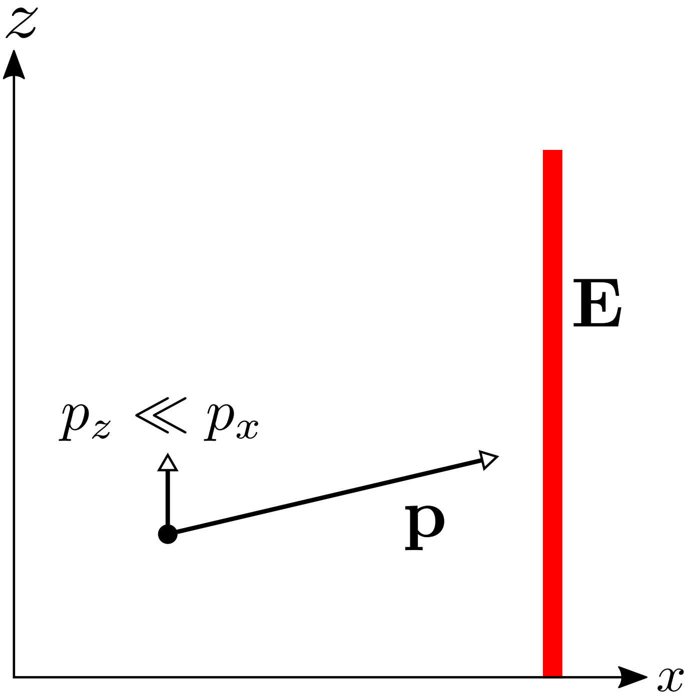

Figure 1.1: Interaction of an atom with a beam of light of frequency ω_L and wavenumber k_L. An atom interacting with such a field will affect in general both the internal state and the momentum state, as the atom will recoil when absorbing a photon. Image adapted from [3].

is that we can treat the space-varying Rabi frequency $\Omega(x)$ as a time-varying quantity by changing reference frame $\Omega(x \approx v_x t) = \Omega(t)$.

We can then treat the problem as we did in 1.1.1: writing the Schrödinger equation for the atomic Hamiltonian (we will denote $|g, p_z\rangle$ with $|g, 0\rangle$)

$$\begin{cases} \mathscr{H}\,|g,0\rangle = \dfrac{\hat{p}^2}{2m}\,|g,0\rangle \\ \mathscr{H}\,|e,1\rangle = \left(\dfrac{(\hat{p}+\hbar k_L)^2}{2m} + \hbar\omega_{eg}\right)|e,+1\rangle\,, \end{cases} \tag{1.5}$$

the interaction Hamiltonian (1.2), and the state

$$|\Psi(t)\rangle = a(t)e^{-i\omega_{g,0}t}\,|g,0\rangle + b(t)e^{-i\omega_{e,+1}t}\,|e,+1\rangle\,,$$

where $a(t) = \alpha(t)e^{i\omega_{g,0}t}$ and $b(t) = \beta(t)e^{i\omega_{e,1}t}$ are such that $|\Psi(t)\rangle = \alpha(t)|g,0\rangle + \beta(t)|e,1\rangle$, we find the differential equations for the coefficients:

$$\begin{cases} \dot{a}(t) = +i\dfrac{\Omega(t)}{2}e^{i\Delta t}b(t) \\ \dot{b}(t) = i\dfrac{\Omega(t)}{2}e^{-i\Delta t}a(t); \end{cases} \tag{1.6}$$

the energy diagram for the problem can be seen in figure 1.2. The detuning Δ in Eq. (1.6) is different from the one that we found previously; this is due to the motion of the atoms:

$$\begin{aligned} \Delta &= \omega_L + \omega_{g,0} - \omega_{e,+1} \\ &= \underbrace{\omega_L - \omega_{eg}}_{\delta} - \underbrace{\frac{k_L p_z}{m}}_{\omega_D} - \underbrace{\frac{\hbar k_L^2}{2m}}_{\omega_R}. \end{aligned}$$

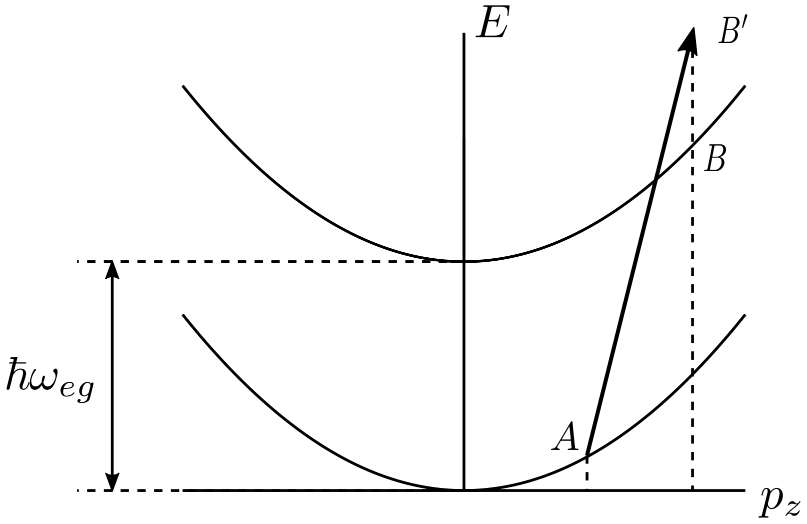

Figure 1.2: Energy diagram for the problem of the scattering of one atom from a laser beam, as written in Eq. (1.5). There is a difference between B and the energy of the excited state B'; this energy difference is the detuning Δ of the laser, as seen in the atom's reference, and it has a constant part and a part linear with p_z: this latter term is the Doppler shift for the moving atom. Image adapted from [3].

Now that the problem for a single (i.e. travelling) wave is solved, we can solve the problem for the scattering of an atom by a standing wave, that is the superposition of two travelling waves. The interaction Hamiltonian is

$$\mathscr{H}_i = \frac{\hbar\Omega}{2}\left(e^{ik_Lz} + e^{-ik_Lz}\right)\left(e^{i\omega_Lt}\left|g\right\rangle\left\langle e\right| + e^{-i\omega_Lt}\left|e\right\rangle\left\langle g\right|\right). \tag{1.7}$$

We can see that the $|g,0\rangle$ level is coupled by the field to $|e,\pm1\rangle$, and that these states are, in turn, coupled to $|g,\pm2\rangle$, and so $|g,0\rangle$ is coupled to all $|g,\pm2n\rangle$. Because we assume coherent scattering, this process is just a redistribution of photons from one beam to another, and the total energy of the system composed by atom and beams is conserved.[2]

If the atomic internal state is not changed by light scattering, the energy conservation means that there is no change in the kinetic energy of the atom, that is

$$|\boldsymbol{p}| = |\boldsymbol{p} + 2n\hbar\boldsymbol{k}_L|, \tag{1.8}$$

but we also see that, if $\boldsymbol{p} \parallel x$ and $\boldsymbol{k}_L \parallel z$, the vectors $\boldsymbol{p}$ and $\boldsymbol{p} \pm 2\hbar\boldsymbol{k}_L$ cannot have the same modulus, as Eq. (1.8) would require. In order to solve this problem, we shall consider a more realistic laser beam: the *Gaussian beam*, which has an intensity profile

$$I(x,y,z) \propto e^{-2\frac{x^2+y^2}{w^2(z)}},$$

and the *beam waist* $w^2(z)$ is, taking $z = 0$ in its minimum,

$$w^2(z) = w_0^2\left[1 + \left(\frac{z}{z_R}\right)^2\right],$$

where $z_R = \pi w_0^2/\lambda$ is called *Rayleigh range* [6, P. 153].[3] This beam has a component along x, and so the process becomes possible, as long as w_0 is small enough. This regime is called the *Raman-Nath regime*,[4] and implies that $p_z^2/2m \approx 0$. If w_0 is instead sufficiently big, we can take $\boldsymbol{p}$ and $\boldsymbol{p} + 2\hbar\boldsymbol{k}_L$ symmetric with respect to x, and $\boldsymbol{k}_L \parallel z$; this is called the Bragg regime. Physically speaking, we can say that Bragg scattering is more similar to an

---

[2] The assumption of coherent scattering is valid as long as incoherent, i.e. spontaneous, emission is negligible.

[3] The Rayleigh range is the value of z for which the beam waist is $\sqrt{2}w_0$.

[4] Also known as Kapitza-Dirac scattering, as the paper [7] treated the diffraction of an electron from a standing wave.

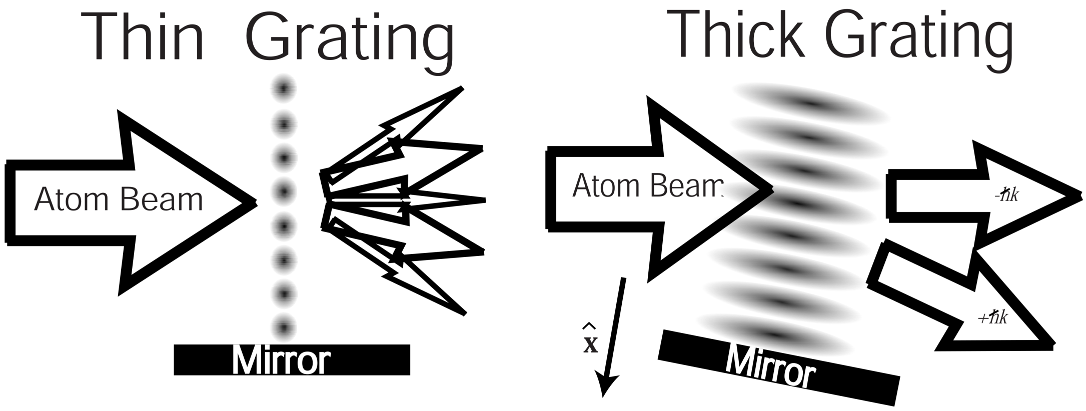

Figure 1.3: Comparison between the Bragg and Raman-Nath regimes of atomic diffraction, from [1]. The latter, on the left, can be seen as the diffraction from a thin grating: as in the familiar optical case, we have multiple diffraction orders with different intensities. The Bragg scattering is the scattering from a thick grating that is weakly perturbing: in this case, a familiar analogue would be the scattering of a light wave from a crystal, and we have, as we expect, diffraction when $\boldsymbol{k}_i - \boldsymbol{k}_f = \boldsymbol{G}$, where k_i and k_f are the initial and final wavevectors, and $\boldsymbol{G}$ is a reciprocal lattice vector for the grating.

optical beam splitter, as the beam is divided in two components, whereas the Raman-Nath scattering is more similar to the effect of a diffraction grating, as the incident beam is divided into a symmetric fan of impulse states. This argument can be also compounded by the consideration that, if the pulse duration is brief compared to $\hbar/E_R$, where $E_R = \hbar^2 k_L^2/2m$ is the recoil kinetic energy, by Heisenberg's uncertainty principle the energy transferred with that pulse must have a large uncertainty: if this energy spread is sufficient to populate other states, we have the Raman-Nath regime, otherwise we are in the Bragg regime. A comparison between the two regimes can be seen in figure 1.3.

1.1.3 Raman-Nath Regime

If the kinetic energy along the z axis is neglected, all the terms in the Hamiltonian commute with z, and thus z is a constant of motion, and we can make all our calculation taking $\mathcal{H}_i(z)$ of equation (1.7) as $\mathcal{H}_i(z_0)$.

In the off-resonance case, we can easily calculate the probability of finding the atom in the $n-$th diffracted order, following [8]. An off-resonance electric field creates a potential, called *optical dipole potential*, that can be explained with the different AC Stark shifts for the ground and excited level [9]. The potential for the atom-field system (1.7) can be written as

$$V(z,t) = \hbar \frac{\Omega^2(t)}{\Delta} \cos^2(k_L z). \tag{1.9}$$

Being off resonance, we can assume that the atom remains in the state $|g\rangle$, and, therefore, we can write the final state as

$$|\Psi_f\rangle = |g\rangle \exp\left[-\frac{i}{\hbar}\int_{\mathbb{R}} \mathrm{d}t\, V(z,t)\right]. \tag{1.10}$$

We define

$$\bar{\Omega}^2(z) = \frac{1}{\tau}\int_{\mathbb{R}} \mathrm{d}t\, \Omega^2(z,t),$$

where τ is the transit time, i.e. the time interval for which Ω is appreciably different from 0, and thus Eq. (1.10) becomes

$$|\Psi_f\rangle = |g\rangle\, e^{-i\frac{\bar{\Omega}^2\tau}{2\Delta}(1-\cos(2k_L z))};$$

we expand in terms of the Bessel functions of first kind:

$$\begin{aligned} |\Psi_f\rangle &= |g\rangle\, e^{-i\frac{\bar{\Omega}^2\tau}{2\Delta}} \sum_{n=-\infty}^{+\infty} i^n J_n\left(\frac{\bar{\Omega}^2\tau}{2\Delta}\right) e^{-i2nk_L z} \\ &= e^{-i\frac{\bar{\Omega}^2\tau}{2\Delta}} \sum_{n=-\infty}^{+\infty} i^n J_n\left(\frac{\bar{\Omega}^2\tau}{2\Delta}\right) |g, 2n\hbar k_L\rangle. \end{aligned}$$

Therefore, the probability for diffraction in the order n is

$$P_n = J_n^2\left(\frac{\bar{\Omega}^2\tau}{2\Delta}\right).$$

1.1.4 Bragg regime

In the Bragg regime, the waist of the beam is big and, therefore, we can consider it as a thick grating. Given that, as said above, $\boldsymbol{p}$ and $\boldsymbol{p} + 2\hbar\boldsymbol{k_L}$ must be symmetric with respect to the x axis, the two states of interest are $|g,-1\rangle$ and $|g,+1\rangle$. Following the treatment in [8], we consider this as a two level system undergoing a two photon transition, also called a *stimulated Raman transition*. The atomic Hamiltonian is

$$\mathcal{H}_a = \hbar\omega_L\,|e,0\rangle\,\langle e,0| + \frac{\hbar^2 k_L^2}{2m}\,|g,-1\rangle\,\langle g,-1| + \frac{\hbar^2 k_L^2}{2m}\,|g,+1\rangle\,\langle g,+1|\,,$$

the interaction Hamiltonian

$$\mathcal{H}_i = -ie^{-i\omega_L t}\frac{\hbar\Omega}{2}\,(|e,0\rangle\,\langle g,-1| - |e,0\rangle\,\langle g,-1|) + h.c.$$

and we search a solution for the Schrödinger equation of the form

$$|\Psi\rangle = \alpha\,|g,-1\rangle\,e^{-i\frac{\hbar k_L^2}{2m}t} + \beta\,|g,+1\rangle\,e^{-i\frac{\hbar k_L^2}{2m}t} + \gamma\,|e,0\rangle\,e^{-i\omega_{eg}t}.$$

The population of the $|e,0\rangle$ state, when the radiation is off-resonance with the atomic transition, is negligibly small, and so we can put $\gamma \approx 0$. Solving the differential equations for α and β with the initial conditions $\alpha(0) = 1$, $\beta(0) = 0$, we obtain the result

$$\begin{aligned}\alpha(t) &= e^{-i\frac{\Omega^2}{4\Delta}t}\cos\left(\frac{\Omega_R^2}{4\Delta}t\right)\\ \beta(t) &= e^{-i\frac{\Omega^2}{4\Delta}t}\sin\left(\frac{\Omega_R^2}{4\Delta}t\right),\end{aligned}$$

where we see that the Rabi oscillations occur at the *two photon Rabi frequency*,

$$\Omega_{(2)} = \frac{\Omega^2}{2\Delta}.$$

The transition probability, considering that the transit time is τ, is

$$P(\tau) = \sin^2\left(\frac{\Omega_{(2)}}{2}\tau\right). \tag{1.11}$$

Even with the result of Eq. (1.11), we should be wary of the two level approximation in this case, as $|g,+1\rangle$ is coupled not only to $|g,-1\rangle$, but also to $|g,+3\rangle$. The condition

$$\tau \gg \frac{\pi}{2\omega_R}$$

assures that the interaction time is enough to resolve the frequency difference from the first to the second Bragg order [8]. The other key concern is spontaneous emission, which results in an incoherent scattering. From [9], we see that the rate of spontaneous emission is

$$A = \Gamma_a \frac{\Omega^2}{4\delta^2},$$

where Γ_a is the rate of spontaneous emission for the unperturbed atom. Therefore, we shall limit the region for Bragg scattering to $A\tau \ll 1$. Another key limit is that the depth of the potential in Eq. (1.9) is smaller than the recoil energy $\hbar^2 k_L^2/2m$ of the atom, in order to be able to consider the potential as a perturbation of the atom; if this condition is not fulfilled, we enter the *channelling regime*, in which the atoms are simply guided as they go through the grating along the minima of the potential [1].[5]

1.2 Wave function of a BEC

Bose-Einstein condensation is defined, in the broadest terms possible, as the macroscopic occupation of the ground state of a system. Following the treatment of [10], we write the many-body field operator

$$\hat{\Psi}(\boldsymbol{r}) = \phi_0(\boldsymbol{r})\hat{a}_0 + \sum_{i\neq 0} \phi_i(\boldsymbol{r})\hat{a}_i, \tag{1.12}$$

where the ϕ_i are the single particle states, and $\hat{a}_i$ is the annihilation operator for a particle in the $i-$th state. If the number of particles in the ground state, $\langle a_0^\dagger a_0 \rangle = N_0$, is large, it is justified [10] to approximate

$$\begin{aligned} \hat{a}_0^\dagger &\approx \sqrt{N_0} \\ \hat{a}_0 &\approx \sqrt{N_0}; \end{aligned}$$

this is called the *Bogoliubov approximation*. Equation (1.12) thus becomes

$$\hat{\Psi} = \Psi_0 + \sum_{i\neq 0} \phi_i \hat{a}_i,$$

---

[5] This is, in principle, also valid for the Raman-Nath case; however, due to the thinness of the grating, this becomes less relevant.

and $\Psi_0 = \sqrt{N_0}\phi_0$ is therefore the order parameter that characterizes the Bose-Einstein condensate; it is equal to 0 above a certain temperature, and goes to $\sqrt{N}\phi_0$ as $T \to 0$ [11]:

$$N_0 = N\left[1 - \left(\frac{T}{T_c}\right)^{\alpha}\right],$$

where α depends on the confinement of the condensate. We shall thus seek a description of the condensate in terms of Ψ_0.

1.2.1 The Gross-Pitaevskii equation

In order to have an equation for the evolution of Ψ_0, we should begin from the Hamiltonian

$$\mathscr{H} = -\frac{\hbar^2\nabla^2}{2m} + V_e(\boldsymbol{r},t) + \int_{\mathbb{R}^3} \mathrm{d}\boldsymbol{r}' \hat{\Psi}^\dagger(\boldsymbol{r}')V(\boldsymbol{r}-\boldsymbol{r}')\hat{\Psi}(\boldsymbol{r}'); \tag{1.13}$$

where V_e is an external potential, and the last term is the direct Hartree term that keeps track of the interactions between two particles in a condensate. We can approximate further this interaction in order to have it in terms of Ψ_0, by noting that, at low energy, the scattering properties are governed by a constant term in momentum space [11],

$$g = \frac{4\pi\hbar^2 a}{m},$$

that means that the two-body interactions can be replaced by an appropriate contact potential

$$V(\boldsymbol{r}) = g\delta(\boldsymbol{r}-\boldsymbol{r}'),$$

where a is the s-wave scattering length for the original interaction. By using this contact potential in Eq. (1.13) and writing the Heisenberg equation, we obtain

$$i\hbar\frac{\partial}{\partial t}\Psi_0 = \left(-\frac{\hbar^2\nabla^2}{2m} + V_e(\boldsymbol{r},t) + g|\Psi_0|^2\right)\Psi_0;$$

this equation is the *Gross-Pitaevskii equation* (GPE), and describes the behaviour of a Bose-Einstein condensate. If we suppose a stationary wave function

$$\Psi_0 = \psi(\boldsymbol{r})e^{-i\frac{\mu}{\hbar}t},$$

we obtain the time-independent GPE

$$\left(-\frac{\hbar^2\nabla^2}{2m} + V_e(\boldsymbol{r}) + g|\psi|^2\right)\psi = \mu\psi. \tag{1.14}$$

If we calculate the energy functional for the state $|\psi\rangle$:

$$E[\psi] = \frac{\langle\psi|\,\mathcal{H}_{GP} - \mu\,|\psi\rangle}{\langle\psi||\psi\rangle},$$

where $\mathcal{H}_{GP}$ is the Hamiltonian in Eq. (1.14), and we impose the variational condition $\delta E[\psi] = 0$, we can prove that the μ in Eq. (1.14) is indeed the chemical potential for the system [12]:

$$\mu = \frac{\partial E}{\partial N},$$

where E is the energy of the state for which the energy functional is stationary.

1.2.2 Interference with BEC

Suppose that we have a condensate delocalized on two points separated by a distance $\boldsymbol{d}$ and that between them the relationship

$$\Psi(\boldsymbol{r},0) = \Psi_a\left(\boldsymbol{r} - \frac{\boldsymbol{d}}{2}, 0\right) + e^{i\Phi}\Psi_b\left(\boldsymbol{r} + \frac{\boldsymbol{d}}{2}, 0\right)$$

holds [10], with d large enough that the spatial overlap of Ψ_a and Ψ_b is negligible. Now, if the condensate starts expanding freely at $t = 0$, after some time we will have

$$n(\boldsymbol{r},t) = n_a(\boldsymbol{r},t) + n_b(\boldsymbol{r},t) + 2\sqrt{n_a n_b}\cos\left(S(\boldsymbol{d},t) + \Phi\right), \tag{1.15}$$

where $n = |\Psi|^2$. There is therefore a modulation in the density of the condensates, that is due to an interference effect: this is the conceptual basis for interferometry with BEC.

1.2.3 Ideal Bose-Einstein wave function

The Gross-Pitaevskii equation is in general of difficult solution, because of the self-interaction of Ψ_0, but we can see that, in the simplest case of $g = 0$, Eq.

(1.14) becomes nothing more than the Schrödinger equation. In the case of greater interest, both from an experimental and a theoretical point of view, of an harmonic potential,

$$V_h(x,y,z) = \frac{1}{2}m\omega_x x^2 + \frac{1}{2}m\omega_y y^2 + \frac{1}{2}m\omega_z z^2$$

we have the wave function [11]

$$\psi(\boldsymbol{r}) = \frac{1}{\sqrt{\pi^{3/2}a_x a_y a_z}} e^{-\left(\frac{x^2}{2a_x^2}+\frac{y^2}{2a_y^2}+\frac{z^2}{2a_z^2}\right)},$$

where the characteristic lengths a_i ($i = x,y,z$) are

$$a_i = \sqrt{\frac{\hbar}{m\omega_i}},$$

and

$$\psi(\boldsymbol{k}) = \frac{1}{\sqrt{\pi^{3/2}b_x b_y b_z}} e^{-\left(\frac{\hbar^2 k_x^2}{2b_x^2}+\frac{\hbar^2 k_y^2}{2b_y^2}+\frac{\hbar^2 k_z^2}{2c_z^2}\right)}, \tag{1.16}$$

with $b_i = \hbar/a_i$. If now we release the trap, the momentum components of Eq. (1.16) are [11]

$$\Psi(\boldsymbol{k},t) = \psi(\boldsymbol{k})e^{-i\frac{\hbar^2 k^2}{2m}\frac{t}{\hbar}},$$

and thus

$$\begin{aligned}\Psi(\boldsymbol{r},t) &= \frac{1}{\sqrt{8\pi^3}}\int_{\mathbb{R}^3} \mathrm{d}\boldsymbol{k}\, \exp\left[-\frac{\hbar^2\boldsymbol{k}^2}{2b^2} - i\frac{\hbar^2\boldsymbol{k}^2}{2m}\frac{t}{\hbar}\right]e^{i\boldsymbol{k}\cdot\boldsymbol{x}}\\ &= \prod_{i=x,y,z}\frac{1}{[\pi a^2(1+i\omega_i t)]^{1/4}}e^{-\frac{r_i^2}{2a^2(1+i\omega_i t)}}\end{aligned}$$

The BEC therefore expands, and the expansion velocity is proportional, for large t, to the frequency of the trap, i.e. the expansion is fastets in the most confined directions.

1.2.4 Interacting Bose-Einstein wave function

The evolution of a BEC wave function can also be treated in an interacting case. In order to achieve this, the first step is to introduce the *Thomas-Fermi approximation:* in this approximation, the kinetic energy term is ignored in Eq. (1.14), leading to [11]:

$$\left[V_e(\boldsymbol{r}) - Ng|\psi|^2\right]\psi = \mu\psi,$$

that has the simple solution

$$\psi_{TF}(\boldsymbol{r}) = \sqrt{\frac{\mu - V(\boldsymbol{r})}{gN}},$$

and the chemical potential is found by normalizing the wave function

$$\mu = \frac{1}{2}\hbar\bar{\omega}\left(15Na\sqrt{\frac{m\bar{\omega}}{\hbar}}\right)^{2/5},$$

where $\bar{\omega} = \sqrt[3]{\omega_x\omega_y\omega_z}$ is the geometric mean of the trapping frequencies. Following [13], we will derive the equations that describe the expansion of the Thomas-Fermi wave function when in a time-dependent harmonic potential.[6]

Suppose first we have a gas of classical particles with the potential

$$V_h(\boldsymbol{r},t) + g\rho(\boldsymbol{r},t),$$

where ρ is the density of the gas. The gas will evolve by expanding in some way, and therefore we can make the ansatz

$$r_i(t) = \lambda_i(t) r_i(0), \qquad j = x,y,z, \tag{1.17}$$

that results in a ρ of the form

$$\rho(\boldsymbol{r},t) = \frac{1}{\Lambda(t)}\rho\left(\left(\frac{r_x}{\lambda_x}, \frac{r_y}{\lambda_y}, \frac{r_z}{\lambda_z}\right), 0\right),$$

---

[6] The most important special case for this problem is the release of the condensate from a trap, that is treated by using for the time dependant harmonic frequency,

$$\omega_i(t) = \begin{cases} \omega_i & t \leq 0 \\ 0 & t > 0 \end{cases} \qquad i = x,y,z.$$

with $\Lambda(t) = \lambda_x(t)\lambda_y(t)\lambda_z(t)$. The Newton equation for the system is

$$mr_i(0)\frac{\mathrm{d}^2}{\mathrm{d}t^2}\lambda_i(t) = -\frac{\partial}{\partial r_i}V_h(\boldsymbol{r}(t),t) + \frac{1}{\lambda_i(t)}\frac{1}{\Lambda(t)}\frac{\partial}{\partial r_i}V_h(r(0),0);$$

calculating the derivatives we have

$$\frac{\mathrm{d}^2}{\mathrm{d}t^2}\lambda_i(t) + \omega_i^2(t)\lambda_i = \frac{1}{\Lambda(t)}\frac{\omega_i^2(0)}{\lambda_i(t)}; \tag{1.18}$$

these equations describe the evolution of the λ_i, and , for this reason, are called *scaling equations*. From (1.17) we also obtain the local velocity in the expanding cloud:

$$v_i(\boldsymbol{r},t) = r_i\frac{\dot{\lambda}_i(t)}{\lambda_i(t)} \tag{1.19}$$

The important aspect of these equations is that they do not depend on the interaction parameter, apart from the constant term N_0. This means that, in the Thomas-Fermi limit, the effect of the interactions is to determine the initial shape of the wave function, that will then expand like an ideal gas.

Returning to the BEC, we can use equations (1.17) and (1.19) and make the assumption that Eq. (1.17) will hold. We will have therefore

$$\Psi(\boldsymbol{r},t) = \exp\left[-i\beta(t) + i\frac{m}{2\hbar}\sum\frac{\dot{\lambda}_i^2(t)}{\lambda_i(t)}r_i^2\right]\frac{1}{\sqrt[3]{\Lambda(t)}}\tilde{\Psi}\left(\left(\frac{r_x}{\lambda_x},\frac{r_y}{\lambda_y},\frac{r_z}{\lambda_z}\right),0\right).$$

By inserting this wave function in the GPE and then doing the Thomas-Fermi approximation, we obtain that

$$n_{TF}(\boldsymbol{r},t) = \frac{1}{\Lambda(t)}\left(\frac{\mu}{g} - \frac{1}{g}\sum_i\frac{1}{2}m\omega_i^2(0)\frac{r_i^2}{\lambda_i^2}\right);$$

the λ_i still evolve with the equation (1.18).

A simple but interesting solution for Eq. (1.18) can be found when we have an elongated trap, with $\omega_x = \omega_y \gg \omega_x$, that is released at $t = 0$, $\omega_i(t > 0) = 0$. For this problem, the scaling equations are:

$$\begin{cases} \frac{\mathrm{d}^2}{\mathrm{d}t^2}\lambda_x = \frac{\omega_x^2(0)}{\lambda_x^3\lambda_z} \\ \frac{\mathrm{d}^2}{\mathrm{d}t^2}\lambda_z = \frac{\omega_z^2(0)}{\lambda_x^2\lambda_z^2} \end{cases}$$

and approximate solutions are

$$\begin{cases}\lambda_x(t) \approx \sqrt{1+(\omega_x(0)t)^2} \\ \lambda_z(t) \approx 1+\dfrac{\omega_z(0)^2}{\omega_x(0)^2}\left(\omega_x(0)t\arctan(\omega_x(0)t) - \ln\sqrt{1+(\omega_x(0)t)^2}\right).\end{cases}$$

1.3 Phase evolution

If we start from a single wave packet that is then split onto the two paths, the interference fringes in Eq. (1.15) will be due to the differential evolution in the two arms of the interferometer. This difference may be caused either by the interaction of the particle with a different field in the two arms, or by difference in the geometry of the two paths.

The most useful formalism for the calculation of a phase shift is that of *Feynman's path integrals*. Given an initial wave function $\Psi(\boldsymbol{r}_i,t_i)$ and a final wave function $\Psi(\boldsymbol{r}_f,t_f)$, we have that [14]

$$\begin{aligned}\Psi(\boldsymbol{r}_f,t_f) &= \langle\boldsymbol{r}_f|\,|\Psi(t_f)\rangle \\ &= \langle\boldsymbol{r}_f|\,U(t_i,t_f)\,|\Psi(t_i)\rangle \\ &= \int \mathrm{d}\boldsymbol{r}_i K(\boldsymbol{r}_i,t_i,\boldsymbol{r}_f,t_f)\,\Psi(\boldsymbol{r}_i,t_i).\end{aligned} \tag{1.20}$$

The operator K is called the *propagator* for the wave function, and it is the solution to the equation [15]

$$\left[-i\hbar\frac{\partial}{\partial t_f} - \frac{\hbar^2}{2m}\nabla_f^2 + V(\boldsymbol{r}_f)\right]K(\boldsymbol{r}_i,t_i,\boldsymbol{r}_f,t_f) = \delta(\boldsymbol{x}_f-\boldsymbol{x}_i)\,\delta(t_f-t_i).$$

Feynman's idea was to express the integral in Eq. (1.20) as

$$K(\boldsymbol{r}_i,t_i,\boldsymbol{r}_f,t_f) = \sum_{\{\Gamma\}} e^{i\frac{\mathscr{S}(\Gamma)}{\hbar}}, \tag{1.21}$$

where $\{\Gamma\}$ is the set of all the paths Γ from $(\boldsymbol{r}_i,t_f)$ to $(\boldsymbol{r}_f,t_f)$, $\mathscr{S}(\Gamma)$ is the action calculated along Γ:

$$\mathscr{S}(\Gamma) = \int_\Gamma \mathrm{d}t\,\mathscr{L}(\boldsymbol{r}(t),\dot{\boldsymbol{r}}(t),t),$$

and $\mathscr{L}$ is the Lagrangian of our system. It can be shown that, for paths with a substantial deviation from the classical path $\mathit{\Gamma}_c$, the exponential term in Eq. (1.21) oscillates rapidly, and therefore the contribution of those paths to the integral vanish. If we have a perturbation in the Lagrangian $\mathscr{L} = \mathscr{L}_0 + \epsilon\mathscr{L}_1$, we can write [14]

$$\mathit{\Psi}(\boldsymbol{r}_f, t_f) = \mathit{\Psi}_0(\boldsymbol{r}_f, t_f)e^{i\phi},$$

where $\mathit{\Psi}_0$ is the unperturbed wave function and

$$\phi = \frac{\epsilon}{\hbar}\int_{\mathit{\Gamma}_c} \mathrm{d}t\, \mathscr{L}_1(\boldsymbol{r}, \dot{\boldsymbol{r}}, t)$$

is the action calculated along the classical path for the perturbation only.

This last equation is therefore suitable for treating the phase evolution of a wave packet that travels along one of the two arms of an interferometer. If the path along the first arm is ABC, and that along the second arm is $AB'C$, then [14]

$$\phi = \frac{\epsilon}{\hbar}\oint_{ABCB'A} \mathrm{d}t\, \mathscr{L}_1.$$

1.4 Atom interferometry

Now that we have some knowledge of all the principal elements of an atomic interferometer, we can discuss how all these pieces come together, and what are some possible uses for this technique.

While the general scheme for the realization of an atomic interferometer is identical to that of an optical one, there are some special considerations that have to be made when using matter waves. One of the first considerations it that the two length scales for an interferometry experiment, namely the wavelength and the (longitudinal) coherence length of the incoming waves, are much smaller than for light. For example, we could compare a very good incoherent source, an ^{86}Kr discharge lamp, has a wavelength of approximately 6×10^{-7} m and a coherence length of order 1×10^{-1} m, whereas a thermal atomic beam has a wavelength of order 1×10^{-11} m and a coherence length of order 1×10^{-10} m [1]. For coherent sources, the wavelength of a He-Ne laser is about the same as that of the ^{86}Kr lamp, but its coherence length can easily be brought to an order of 1×10^{2} m [16], but for a BEC, it can rarely exceed 1×10^{-5} m, and the condensate has maximum wavelength of order 1×10^{-6} m. Another consideration is that the atoms in a BEC or in a thermal beam interact with one another much more strongly than the photons in a light beam, giving rise to non linear effects. Moreover, if condensates are used, there is a minimum time between two interrogations of the interferometer, because of the time needed to prepare the condensate.[7]

1.4.1 The Mach-Zehnder and Ramsey interferometers

In optics, a Mach-Zehnder interferometer is formed by a beam splitter that divides the incoming beam into two paths, which then are reflected by mirrors onto a second beam splitter, that recombines them (figure 1.4, left). By placing in one arm a substance with a diffraction index n_2, different from the diffraction index of the working medium n_1,[8] the phase difference causes a displacement of the interference fringes with respect those that appear without the n_2 substance. The displacement is [17]

$$\Delta m(x,y) = \int \mathrm{d}z\, n_2(x,y,z) - n_1,$$

where z is the optical axis and n_1 is supposed uniform for simplicity. One of the peculiarities of the Mach-Zehnder interferometer is that it is still capable of producing interferometric fringes even with white light: the dispersion would normally result in a spread of the interference fringes, that overlap until they are not discernible anymore; instead, with this configuration, the spacing of the three central fringes is independent of dispersion [18].

The atomic Mach-Zehnder interferometer uses a conceptually similar arrangement. First, the atoms are split with a grating: while, for the purposes of this thesis, we have treated only light gratings, mechanical gratings such as those used in [19] have also been used with success. This split puts the atoms in a superposition of momentum states: let's take, for simplicity, two states $|g,0\rangle$ and $|g,2\rangle$ obtained with Bragg scattering. Those two states will then evolve freely for a time t_i, when a second pulse will scatter the first state, that moves in the interferometer arm A, to $|g,0\rangle_A$ and $|g,2\rangle_A$, and the second one, in the arm B, to $|g,2\rangle_B$ and $|g,0\rangle_B$. The states $|g,2\rangle_A$ and $|g,2\rangle_B$ can then overlap. Finally, the two waves are imaged after a time t_f, with either an imaging pulse, for condensates, or another kind of detection scheme for thermal atoms. This

---

[7] There are, however, some current efforts to create a continuous beam of condensed atoms [**Chen-2019**].

[8] Usually the working medium is air, but in principle it can work with any medium.

is the interferometric procedure used in this thesis; the whole experimental setup and procedure are detailed in 3.1.

Another kind of interferometer that follows this same idea, but using internal states instead of momentum states is the *Ramsey interferometer*. Ramsey developed this method for the exact determination of atomic frequencies [20], and it is still adopted in the present day definition of the second [21]. Here, the gratings are substituted with a resonant pulse, and the fact that in equation (1.4) the excitation probability is 1 only if $\Delta = 0$ is exploited to stabilize the frequency of the resonant field with that of the atomic transition. In this case, the phase difference in the two atomic paths can be seen as a difference in evolution of the ground state and the excited state, and the fringes are obtained as a function of the detuning.

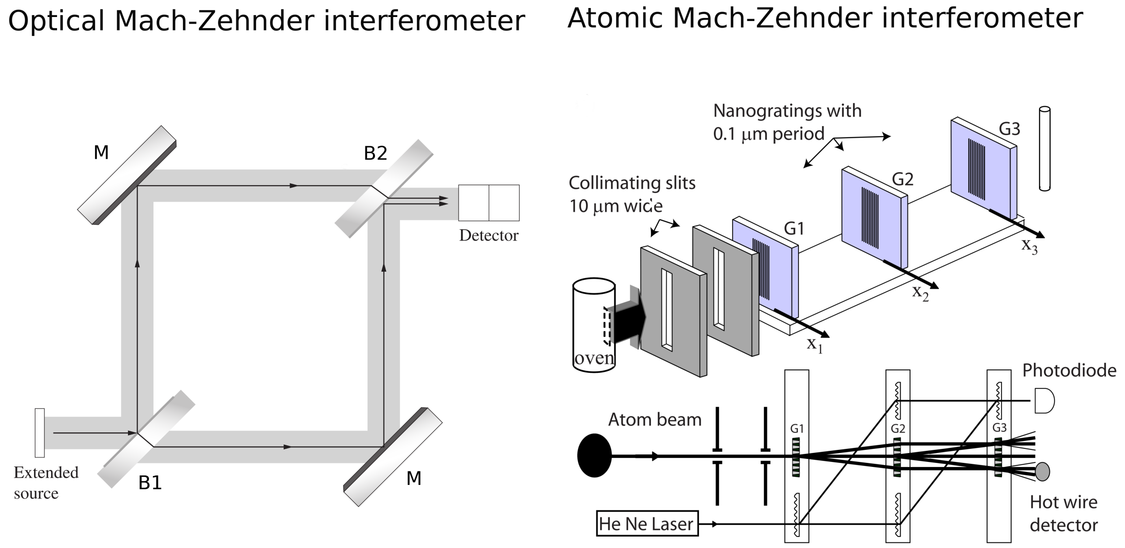

Figure 1.4: Optical (left) and atomic (right) Mach-Zehnder interferometer, as used in [19]. The first beam splitter corresponds to the first grating, and the mirrors correspond to the second, as the light is redirected towards the same point, as the atoms do when they are diffracted the second time. The third is analogous to the second beam splitter, because it makes possible to see the interference pattern by recombining the beams. The image on the left is from [16], the image on the right is from [1].

Bragg interferometer with BEC

The interferometer used in this thesis work is a Bragg interferometer with a BEC. Bragg interferometers are a specialized type of Mach-Zehnder interferometers in which the two beam splitters are Bragg gratings.

In the earlier experiments, condensates were given an initial velocity with a first Bragg pulse [22, 23]. In [22], the first pulse was given by a standing wave that divided the condensate in two components: one at rest, $|0\rangle_1$, and two with a momentum of $\pm 2\hbar k_L$, $|\pm 2\rangle_1$; the components start to separate because of their different momenta. Then, after a time Δt, a second pulse is applied, which further splits the central component in $|\pm 2\rangle_2$ and $|0\rangle_2$: we have thus that $|+2\rangle_1$ and $|+2\rangle_2$ are moving with the same velocity, and along the same path, at a distance $d = \Delta t \cdot 2\hbar k_L/m$. Because they are not trapped, the condensates expand and overlap, thus giving rise to interference. The situation is symmetrical for $|-2\rangle_{1,2}$. All the pulse had a low diffraction efficiency, $P \approx 0.02$, where P is that of Eq. (1.11).

In [23], the two condensates were split by two detuned counterpropagating laser beam detuned from each other. In this way, using a $\pi/2$ pulse, the condensate can be equally split in a rest $|0\rangle_2$ and in a moving $|2\rangle_2$ component, that will then separate. After a time Δt_1, the two components are subjected to a resonant π pulse that will exchange the momenta: $|0\rangle_1 \to |2\rangle_2$ and $|2\rangle_1 \to |0\rangle_2$. Therefore, the two components will start to overlap again. Then, a $\pi/2$ pulse after Δt_2 will again mix the two states in an equal superposition, and they are then imaged.

In the interferometer used in this thesis, the condensate is first given a velocity $v_B = \hbar k_L/m$ by moving the trapping potential. Then, after the potential has been turned off, a $\pi/2$ resonant pulse is applied with an optical lattice; such a pulse puts the original state $|g,+1\rangle$ in an equal superposition $(|g,+1\rangle + |g,-1\rangle)/\sqrt{2}$, and thus the two components of the wave function separate spatially. After a time Δt_i a second, identical pulse completes the interferometer, and each of the incoming state is split again: thus, we now have two $|g,+1\rangle$ and two $|g,-1\rangle$ components. Then, the condensate undergoes a free expansion for a time Δt_f; during this expansion, wave function components with equal momentum progressively overlap, and they separate from those with opposite momentum. Finally, the condensate is imaged. The experimental details are found in Sec. 3.1.

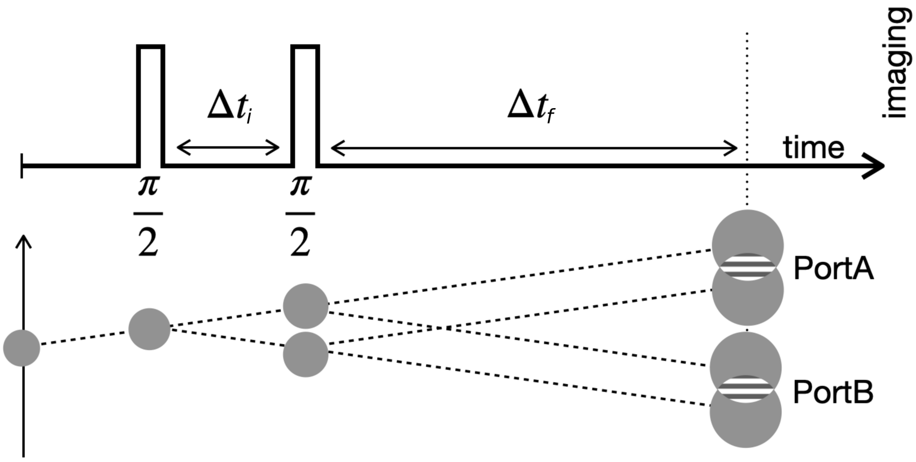

Figure 1.5: Space-time diagram for the Bragg interferometer used in this thesis. Adapted from [24].

1.4.2 Measurements with interferometers

Cold atoms and condensates, due to their small wavelength and narrow line widths of some of their transitions, are especially suited for the implementation of precision measurement protocols. The field of precision measurements with atomic interferometers has been rapidly developing in the past 30 years, and is the subject of a lot of recent and current research; the most recent reviews on the subject are [25] and [26].

Ever since the first demonstration by Kasevich and Chu [27], one of the fields of major utilization of atom interferometry is that of gravitational and inertial forces. Gravimeters are sensor that measure the local gravitational constant g, and are essentially vertical Ramsey interferometers that exploit the Doppler shift caused by the acceleration of the atom in the gravitational field; record sensitivities of approximately $4 \times 10^{-8}\ \mathrm{m/s^2/\sqrt{Hz}}$ have been reached in 2013 [28]. Gradiometers are, instead, instruments apt to measure the gradient of the gravitational field and have reached sensitivities of up to $3 \times 10^{-8}\ \mathrm{/s^2/\sqrt{Hz}}$ [26]. Gyroscopes have been implemented using a matter-wave analogue to the Sagnac effect [29], with the current state of the art being a gyroscope with a sensitivity of $6 \times 10^{-10}\ \mathrm{rad/s/\sqrt{Hz}}$. These techniques have also been used in fundamental studies, such as the measurement of the gravitational constant G, in [30], using a gradiometer and obtaining a relative accuracy of 1.5×10^{-4}, or the confirmation of the equivalence principle of general relativity in [31] up to a factor of 1×10^{-12}.

Another quantity of interest for atomic interferometry is the measurement of magnetic fields, using the spectroscopic detection of the Larmor frequency, which is proportional to the intensity of the magnetic field traversed by the spin ensemble [32]. Sensitivities of approximately $0.5\,\mathrm{fT}/\sqrt{\mathrm{Hz}}$, comparable to those of state-of-the-art SQUID magnetometers, have been achieved, with the advantage of not needing a big cryogenic apparatus [33].

Lastly, all the implementations of atomic clocks use a Ramsey interferometer. While relative clock stabilities $\delta f/f \sim 1 \times 10^{-15}$–$1 \times 10^{-16}$ have been the norm for primary timekeeping for the recent years [34], in recent years there has been a prolific activity in researching atomic transitions that could substitute the hyperfine transition of ^{133}Cs that is used in the current definition of the second, reaching $\delta f/f \sim 2.5 \times 10^{-19}$ by employing ^{87}Sr [35].

We can therefore see that the field of atomic interferometry is a very active field, with many uses for both metrology and precision measurements of fundamental constants. The understanding of the role of the interactions in condensates and the reduction of noise in interferometric images could therefore benefit this discipline.

2

Background removal algorithm

The background removal algorithm we used in this thesis is based on the idea of reconstructing a background of our absorption image, and then subtracting it from our image; a similar approach has been used in other works [36–39].

In section 2.1, we state the problem and give an overview of the absorption imaging of atomic clouds. Then, in 2.2 we describe in detail the various parts of the algorithm. In 2.3 and 2.4 are described, respectively, the methods used to obtain the images we used, and the test we performed on said images, the results of which are reported in 2.5 and briefly discussed in 2.6. The final assessment of the performance of the algorithm is in 2.7. The code for the most relevant functions is shown in appendix A.

2.1 Absorption imaging

Absorption imaging is a widely used technique for the imaging of atomic clouds [40]. When such a cloud with density is illuminated with optical radiation of intensity I_0 and (angular) frequency ω, the transmitted intensity will be:

$$I_t = I_o \exp\left(-\frac{\sigma\tilde{n}(x,y)}{1+\delta^2+\frac{I}{I_s}}\right)$$

[40], where σ_0 is the resonant cross-section,[1] δ is the detuning in units of $\Gamma/2$, and $\tilde{n}(x,y)$ is the *column density*, i.e. the density n integrated in the direction of the beam

$$\tilde{n}(x,y) = \int \mathrm{d}z\, n(\boldsymbol{r}),$$

and finally I_s is the saturation intensity.[2] The transmitted intensity is then captured by a camera, and so we can obtain a two-dimensional map of $\tilde{n}$.

The optical density $D = -\ln(I_t/I_0)$ of an atomic cloud can be as high as 1×10^2 [40] or higher, and so regions of high atomic density can appear uniform when, in fact, they are not. This can be avoided by increasing the δ, which however also causes an increment of the real part of the index of refraction; the refracted radiation degrades the capability for quantitative analysis of the images. It is therefore important to find the right trade-off between the angular resolution and the dynamic range of the absorption image. One of the ways to solve this problem is to make an image of the condensate after some expansion time, during which it is free from all the trapping potentials (time of flight imaging).

From an experimental viewpoint, the optical density is usually obtained by taking three different images: one absorption image of the atomic cloud A, one image of the beam B, and one image C of the dark background. The optical density is then

$$D = -\ln\frac{A-C}{B-C}. \tag{2.1}$$

In both images A and B, there will also be the diffraction figures caused by the optics, which are closer than the coherence length of a laser. These features should in principle exactly cancel in the logarithm, however, in practice, they do not, due to small vibrations in the imaging system, amplitude fluctuations of the probe laser beam, and other factors [36, 38, 39]. There is therefore some residual background noise in the optical density.

---

[1] For a two-level atom and nearly monochromatic light, we have:

$$\sigma_0 = \frac{3\lambda^2}{2\pi}\frac{A}{\Delta\omega},$$

where A is the Einstein spontaneous emission coefficient, and $\Delta\omega$ is the line width of the transition [2]. If the Doppler contribution to $\Delta\omega$ can be neglected, $\Delta\omega = A$, the *natural linewidth* of the atom.

[2] For a two-level atom, $I_s = \frac{\hbar\omega_0 A}{\sigma_0}$ [2]. For ^{87}Rb, the atomic species used in this thesis, in the case of the $|F=2, m_f=\pm 2\rangle \to |F=3, m_f=\pm 3\rangle$ transition, $I_s = (16.69 \pm 0.02)\,\mathrm{W\,m^{-2}}$ [41].

Some efforts have been made to implement *single-shot imaging*, in which the B image is dismissed altogether, and instead an ideal background is reconstructed in other ways: in [36–38], using an algorithm similar to the one we used in this thesis, and in [39] using a deep neural network.

2.2 The algorithm

Background removal algorithms have been studied using different approaches. In our algorithm, similar to [36], a background is reconstructed by calculating a basis of a noise-image space, projecting our image upon said basis, and finally subtracting from our image the linear combination of the noise space basis vectors with the aforementioned weights.

An image is a matrix $\boldsymbol{M}$ in the space of n by m matrices $\mathbb{M}_{n,m}$, where each element A_{ij} is, ideally, proportional to the intensity of optical radiation upon the corresponding pixel of a suitable sensor. The main assumption behind this kind of algorithm is that the noise background can be reasonably approximated in a subspace $\mathbb{N} \subset \mathbb{M}$, and that the signal is contained entirely in another subspace $\mathbb{S} \subset \mathbb{M}$ orthogonal to $\mathbb{N}$. In this way, we could project an arbitrary matrix onto the two subspaces, and keep only the component in $\mathbb{S}$; in practice, this means subtracting from the image $I \in \mathbb{M}$ the component that belongs to $\mathbb{N}$. While we could, in theory, simply train some kind of system to recognize the signal part of the image, in practice this would not be quite impractical, given the ample variety of possible configurations of the atomic cloud. Moreover, a large enough basis for $\mathbb{N}$ would invariably include portions of signal.[3] However, by both our results and results with similar schemes, we can say that this approximation works reasonably well.

Our algorithm will then be:

- acquire as many background images as possible, their number being m;

---

[3] If we take, for example, $\mathbb{M}_{2,2}$, and

$$N_1 = \begin{pmatrix} 1 & 0 \\ 0 & 0 \end{pmatrix}, N_2 = \begin{pmatrix} 0 & 1 \\ 0 & 0 \end{pmatrix},$$
$$N_3 = \begin{pmatrix} 0 & 0 \\ 1 & 0 \end{pmatrix}, S_1 = \begin{pmatrix} 0 & 0 \\ 0 & 1 \end{pmatrix}$$

as the basis vectors for, respectively, $\mathbb{N}$ and $\mathbb{S}$, every part of the image outside of the lower-right pixel would be mapped as noise.

- compute the noise subspace basis from these images ;
- acquire an usual optical-density image;
- project this image on the basis of the noise subspace;
- reconstruct the noise component of our image; and
- subtract the noise from this image.

This procedure is nearly identical to that used by [36–38], because a singular value decomposition is used to compute a basis of the noise space, which is then used to reconstruct the background noise for a particular image; the main difference is that in our case, the algorithm is not used for single-shot imaging, but on an optical density image. Some recent studies have found that this kind of algorithm is susceptible to slow-varying changes in the noise pattern [39]. By doing the denoising on optical density images, we see that this problem is not present, and, as such, an adaptive algorithm is not needed.

2.2.1 Basis calculation

The two main options we considered for this calculation are two different decompositions: QR and singular value decomposition. These matrix decompositions are applied to a matrix $\boldsymbol{M}$ which has for columns the *flattened* images of the background, and then the columns of the matrix that represent the basis vectors of the transformed space are taken as output of the calculation.

The QR decomposition for a matrix $\boldsymbol{A} \in \mathbb{M}_{n,m}$ is of the form

$$\boldsymbol{M} = \boldsymbol{QR},$$

where $\boldsymbol{Q}$ is unitary, and $\boldsymbol{R}$ is upper triangular [42].

The singular value decomposition is a generalization of the widely used diagonal decomposition for matrices of arbitrary shape; it is a factorization of $\boldsymbol{M} \in \mathbb{M}_{n,m}$ of the form

$$\boldsymbol{M} = \boldsymbol{U\Lambda V}^*,$$

where $\boldsymbol{U} \in \mathbb{M}_{n,n}$, $\boldsymbol{V} \in \mathbb{M}_{m,m}$ are unitary matrices, and $\boldsymbol{\Lambda}_{ij} = \delta_{ij}\lambda_j$ is an n by m matrix, whose entries λ_j are called *singular values* [42]. More specifically, the columns of $\boldsymbol{U}$ are the eigenvectors of $\boldsymbol{MM}^*$, those of $\boldsymbol{V}$ are the eigenvectors of $\boldsymbol{M}^*\boldsymbol{M}$, and the λ_j are the p biggest eigenvalues of $\boldsymbol{M}^*\boldsymbol{M}$, with p the number of $\lambda_j \geq 0$ [42].

A possible theoretical advantage of the SVD decomposition over its counterpart is given by the *Eckart-Young-Mirsky theorem* [43].

Definition 1 (Frobenius norm) *For a matrix* $\boldsymbol{M} \in \mathbb{M}_{n,m}$*, the Frobenius norm is defined as:*

$$\|\boldsymbol{M}\|_2 = \sqrt{\sum_{i,j} M_{ij}^2}$$

With this definition, the theorem, as stated in [44] is:

Theorem 1 (Eckart-Young-Mirsky theorem) *For a SVD decomposition of a matrix* $\boldsymbol{M} \in \mathbb{M}_{n,m}$*:*

$$\boldsymbol{M} = \boldsymbol{U}\boldsymbol{\Lambda}\boldsymbol{V}^*,$$

if we define:

- $p \in \mathbb{N}$ *s.t.* $0 \le p \le \min\{n,m\},\ q = n - p$*;*
- $\boldsymbol{U}_1, \boldsymbol{U}_2$ *s.t.* $\boldsymbol{U} = [\boldsymbol{U}_1, \boldsymbol{U}_2]\,, \boldsymbol{U}_1$ *has p columns, and* $\boldsymbol{U}_2$ *has q columns;*
- $\boldsymbol{V}_1, \boldsymbol{V_2}$ *as the analogous partition for* $\boldsymbol{V}$*; and*
- $\boldsymbol{\Lambda}_1 \in \mathbb{M}_{p,p}, \boldsymbol{\Lambda}_2 \in \mathbb{M}_{p,p}$ *s.t.*

$$\boldsymbol{\Lambda} = \begin{pmatrix} \boldsymbol{\Lambda}_1 & \boldsymbol{0} \\ \boldsymbol{0} & \boldsymbol{\Lambda}_2 \end{pmatrix},$$

then $\boldsymbol{M}' = \boldsymbol{U}_1\boldsymbol{\Lambda}_1\boldsymbol{V}_1^*$ *is the matrix for which*

$$\|\boldsymbol{M} - \boldsymbol{M}'\|_2 = \min_{\operatorname{rank}\boldsymbol{B} \le p} \|\boldsymbol{M} - \boldsymbol{B}\|_2\,.$$

In other words, by choosing the appropriate sub-matrices, per the definitions above, we can construct a matrix with lower rank than the original, and the SVD is the optimal algorithm for such an approximation. However, this theoretical advantage does not, necessarily, translate into practice.

In order to choose between the two alternatives, we have compared the denoising performance (2.2) for the two algorithms as a function of various parameters, as described in section 2.4.

2.2.2 Image projection and noise removal

Once the basis $\{\boldsymbol{b}_i\}$ is calculated, we can start by acquiring an optical density image, and then projecting it on the basis. This is done using the usual dot product of the two flattened images, obtaining thus a set of weights:

$$d_i = \boldsymbol{D} \cdot \boldsymbol{b}_i.$$

Then the noise image is reconstructed

$$\boldsymbol{N} = \sum_{i=1}^{q} d_i \boldsymbol{b}_i,$$

and, finally, our clean image will be

$$\boldsymbol{D}_c = \boldsymbol{D} - \boldsymbol{N}$$

2.2.3 Denoising performance

In order to optimize our choices, we have defined a figure of merit, called *denoising performance*, as

$$\begin{aligned} \varDelta(\boldsymbol{D}_c, \boldsymbol{D}) &= \frac{\sigma(\boldsymbol{D}) - \sigma(\boldsymbol{D}_c)}{\sigma(\boldsymbol{D})}, \\ \sigma(\boldsymbol{X}) &= \sqrt{\sum_{i,j \in \mathscr{M}} (X_{ij} - \bar{X}_{i,j})^2} \end{aligned} \tag{2.2}$$

where $\boldsymbol{D}$ and $\boldsymbol{D}_c$ are the images, respectively, before and after the denoising process, $\bar{X}$ indicates the mean of X, and $\mathscr{M}$, called the *masked image*, is the set of the pixels of the image, from which we have removed a central square portion that includes the actual image of the atomic cloud. In other words, the masked image is akin to an external frame of the image, upon which the denoising performance is calculated.

This figure of merit is the difference between the Frobenius norms of the masked two matrices, divided by the Frobenius norm of the first one. In the ideal case, $\boldsymbol{D}_c$ would be exactly equal to zero where there are no atoms, hence maximizing $\varDelta$. Another possibility would have been to define $\varDelta' = \|\boldsymbol{N} - \boldsymbol{D_c}\|_2$, but in this case it would not have been possible to see if a worsening of the noise has occurred, whereas it is possible to do so with (2.2). The masking procedure is necessary, as the maximum of $\varDelta$ would otherwise be for $\boldsymbol{D}_c = \boldsymbol{0}$, but that would go against our goal of improving the absorption images.

2.3 Obtaining the test images

Two kind of images have been used: absorption images of a real condensate, and synthetic images, made by superimposing a noise pattern on a stock image. The synthetic images were employed only for the tests for which it is crucial to control the parameters of the noise (namely, the tests detailed in subsections 2.4.2 and 2.4.1). For all the other tests, we used real images of a Bose-Einstein Condensate, in order to provide a more realistic assessment of the capabilities of the algorithm.

2.3.1 Images of the condensate

The images of the condensate have been obtained following the procedure detailed in 3.1, without carrying out the interferometric sequence. This resulted in images of a spherical Bose-Einstein condensate imaged in free space, like the one reported in 2.3.

2.3.2 Synthetic images

The synthetic images have been made with the [45] image, cropped to 512 px × 512 px, superimposing it on a 1024 px × 1024 px matrix $\boldsymbol{N}$ such that

$$N_{ij} = ar \sin\left(\frac{2\pi n}{1024}\, i\right) + c \tag{2.3}$$

where a is a real parameter, r is a gaussian random variable with mean 0 and variance 1, $n \in \mathbb{N}$ and c is the mean of the signal image. A synthetic image, along with the original, can be seen in figure 2.1.

2.4 Decomposition comparisons

We have made four comparisons of the two decompositions, in order to choose the better one; the first two using synthetic images, and the other two using real images of a BEC. We used the synthetic images so that we could control parameters of the image which would have otherwise been too difficult to manipulate.

Figure 2.1: On the left, the original 512 px×512 px image. On the right, the 1024 px×1024 px image with the synthetic pattern added.

2.4.1 Initial noise

In this test, made using synthetic images and a basis of 30 components, we have varied the parameter a of (2.3), in order to vary the initial RMS value of the noise background.[4] The parameter has been varied in the interval 0.01–1 in steps of 0.01, measuring $\varDelta$ for each of these values.

2.4.2 Spatial frequency

In this test, also made using synthetic images and a basis of 30 components, we have varied the parameter n of (2.3), comparing the performances of the two decompositions for various values of the wavenumber of the noise. The parameter has been varied in the interval 1–512 in steps of 1; the upper bound

---

[4] For an arbitrary signal $s(t)$,

$$s_{\mathrm{RMS}} = \sqrt{\frac{1}{\varDelta t} \int_{\varDelta t} \mathrm{d}t' \, |s(t')|^2},$$

so $(as(t))_{\mathrm{RMS}} = as_{\mathrm{RMS}}$.

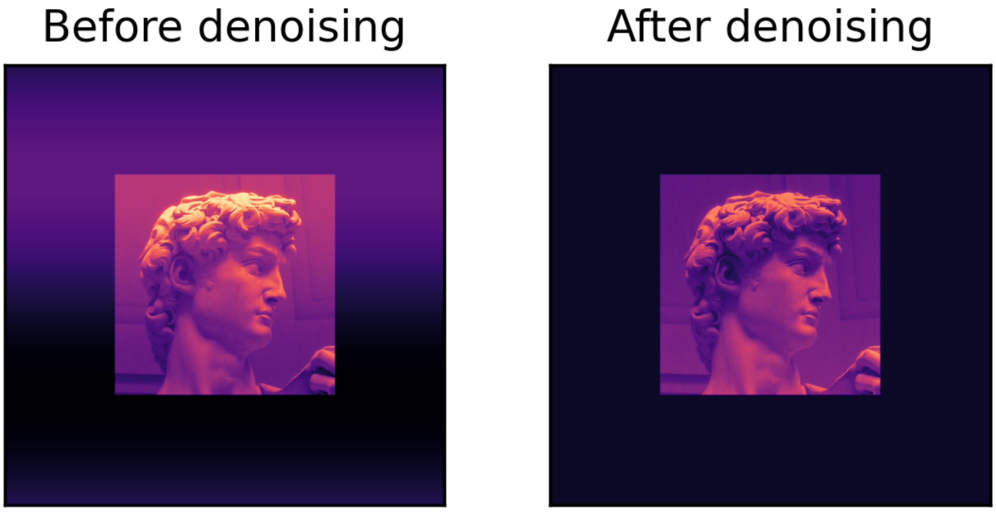

Figure 2.2: On the left, a synthetic image before denoising. On the right, the same image after removal of the background.

of 512 corresponds to the aliasing frequency of the image, whose side is 1024 px. We measured $\varDelta$ for each of these values.

2.4.3 Dimensionality and computation time

For this test, we used 125 real images of a BEC and basis with different numbers of components calculated with backgrounds randomly sampled from a set of 150. We varied the dimensionality of our basis from 1 to 40 in increments of 1, measuring $\varDelta$ for each value. During the same test, we also measured the time required for the two decompositions.

2.5 Results

The algorithm has been seen to work on both synthetic and real images, as can be seen, respectively, in figure 2.2 and in figure 2.3.

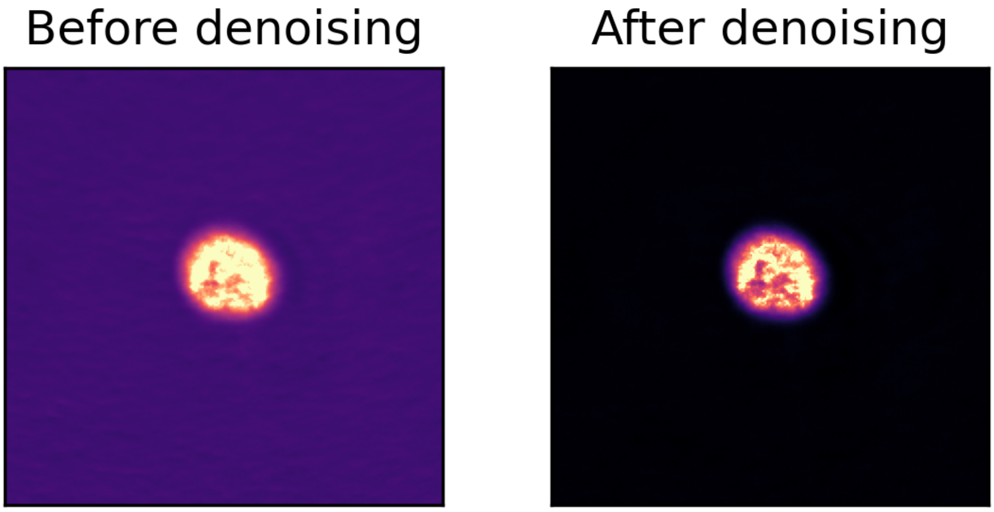

Figure 2.3: On the left, a real image before denoising. On the right, the same image after removal of the background. The images have a 1.7× contrast enhancement.

2.5.1 Initial noise

The two curves acquired are reported in figure 2.4. The mean difference between the two performances $\delta(a) = \Delta_{\text{SVD}}(a) - \Delta_{\text{QR}}(a)$ is 0.0 ± 0.2.[5] Performing a one-sample Student's t-test on δ with null hypothesis that the mean of δ is 0, we find a T-Statistic value of 1.26, with 98 degrees of freedom, and a corresponding p-value of 0.21: we cannot, therefore, reject the null hypothesis.

We can see that, for small values of a, we have a large negative value of Δ. This is due to the fact that the images of the noise basis, which are subtracted from the image, contain a noisy signal. This, under normal circumstances, is the desired behaviour of the denoising algorithm. However, for small amplitudes of the initial noise, the image will still add some noise, as the weight for a component is found to never be exactly zero. Thus, some noise is added to the image, explaining the sign of the Δ. Its magnitude is due to the fact that the initial noise is already very low, and so the added noise can be up to 17 times the initial noise (as can be seen in fig 2.4). In denoising done on real images,

---

[5] Error calculated as standard deviation.

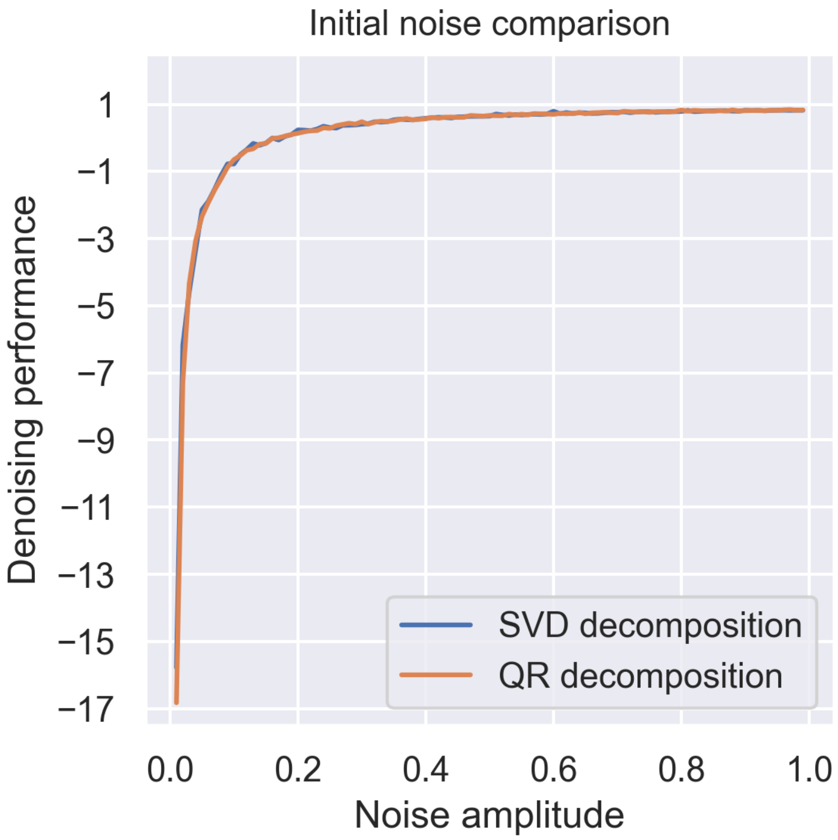

Figure 2.4: Δ as a function of initial noise amplitude, i.e. the parameter a in (2.3). In blue, the SVD decomposition, in orange the QR decomposition.

we always found a positive value of Δ, and as such we can rest assured that real images always have a sufficient amount of noise for the algorithm to be effective.

2.5.2 Noise wavenumber

The two datasets acquired are reported in figure 2.5. For the SVD dataset, we have a mean Δ_{SVD}=0.90 ± 1.00, which is identical to the QR one Δ_{QR}.[6] An

---

[6] Error calculated for both as standard deviation.

independent sample Student's t-test, conducted against the null hypothesis that the two distributions have identical means, finds a T-Statistic of 0.13, with 510 degrees of freedom, and a p-value of 0.89. We therefore do not reject the null hypothesis. A linear regression of Δ as a function of k, suggested by an apparent trend in figure 2.5 finds very weak R^2 coefficients of 0.05 and 0.07 for, respectively, the SVD and QR decompositions.

2.5.3 Dimensionality

The two curves acquired are shown in figure 2.6; their good overlap suggests a very small difference in performance. The mean value of $\delta(n) = \Delta_{\mathrm{SVD}}(n) - \Delta_{\mathrm{QR}}(n)$ is $(7.081\,944 \pm 0.000\,002) \times 10^{-8}$, with the standard error taken as uncertainty. A one sample Student's t-test, against the null hypothesis that this mean value is compatible with 0, results in a t-statistic of 37.8, with 4872 degrees of freedom. The p-value is negligibly different from 0 and we therefore reject the null hypothesis.

We can see that after 10–20 basis components, there is no significant improvement of the performance. Therefore, a conservative value of 20 elements is adequate for our purposes.

2.5.4 Computation time

The two curves acquired are reported in figure 2.7. As can be seen in the graphs, the QR algorithm is usually faster: $t_{\mathrm{QR}} - t_{\mathrm{SVD}}$ is, outside the 29 to 34 component region, between 0.06 s and 0.34 s; however, inside said region, the QR decomposition can be up to 0.97 s slower. At present, we do not have a clear explanation for this quite peculiar behaviour.

2.6 Remarks

The denoising performances of the two algorithm variants are almost identical. Only in one case there has been a statistically significant difference between the two performances: this is probably due to theorem 1. Nevertheless, we chose the SVD algorithm, due to its already proven status in this kind of application [38], and the consideration that, for our application, a decomposition which is marginally slower in the average case is preferable to one that is considerably slower in the worst case.

2.7 Overall performance

The finalized version of the algorithm uses the SVD decomposition and a basis with 20 components. In order to test the overall performance of the algorithm, we used a set of 38 38 images, both of the BEC and of the background, taken much later than the one used until now: in this way, we are sure that there is no noise correlation. We compared the denoising performance to that of the algorithm using the same set of backgrounds used until now, picking each time 20 random images to be diagonalized both for the new and the old background. The results of this comparison can be seen in 2.8. An independent sample Student's t-test, made against the null hypothesis that the two sample have the same average, results in a t-statistic which is 0.81, with 35 degrees of freedom, and a p-value of 0.42. Therefore, we cannot reject the null hypothesis that there is not a significant difference between using background images taken in the same day as the BEC images and others that are over a month older. The problem encountered by [39], that is, the drifting of the noise basis in time, which leads to a diminished denoising performance, is effectively resolved by our approach of denoising images of the optical density.

2.7.1 Comparison with single shot imaging

The algorithm has been compared to the *single shot imaging* method of [36–38]. This algorithm calculates the noise basis using B images[7]. The B image is obtained by the usual weighted sum of the components of the basis, where the weights are given by the projection of the A images upon the various components of the basis. Then, the B image is used to compute the optical density D, resulting in an already denoised image. Using the same raw images used for the calculations of the optical density in the previous test, we performed single shot denoising on all of them. The optical density denoising results in a denoising performance of 0.15 ± 0.11, whereas for the single shot algorithm we have 0.21 ± 0.12.[8] An independent sample Student's t-test results in a statistic of 2.4, with 35 degrees of freedom. Having a p-value of 0.02, we reject the null hypothesis. The single shot method is therefore better, as far as performance is

---

[7] With A and B image we intend thereafter, respectively, $A - C$ and $B - C$ as used in (2.1).

[8] Values of Δ and their respective errors are reported with two significant figures in order to make their difference visible. This is justified by the fact that the two distributions are statistically different.

concerned, than the optical density method presented in this chapter.

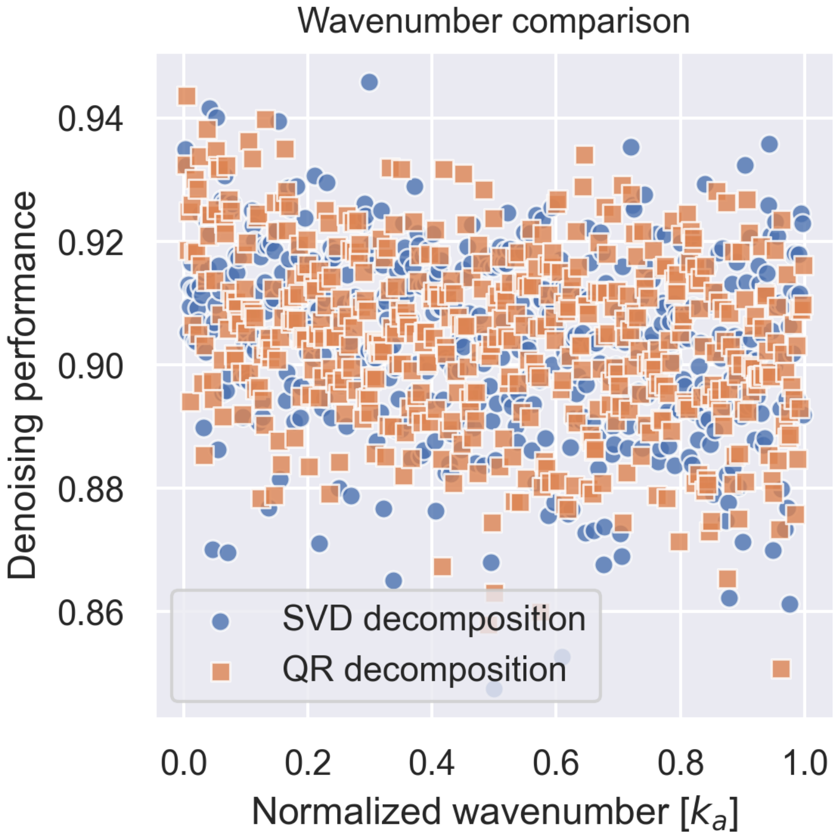

Figure 2.5: Δ as a function of noise wavenumber $k = 2\pi n/1024$ (see (2.3)), in units of normalized aliasing wavenumber $k_a = \pi^{-1}\text{px}^{-1}$, corresponding to a spatial frequency of 0.5 cycles/px, i.e. the frequency that would cause aliasing of the sinusoidal pattern due to the inherently discrete nature of an image made of pixels. In blue, the SVD decomposition, in orange the QR decomposition.

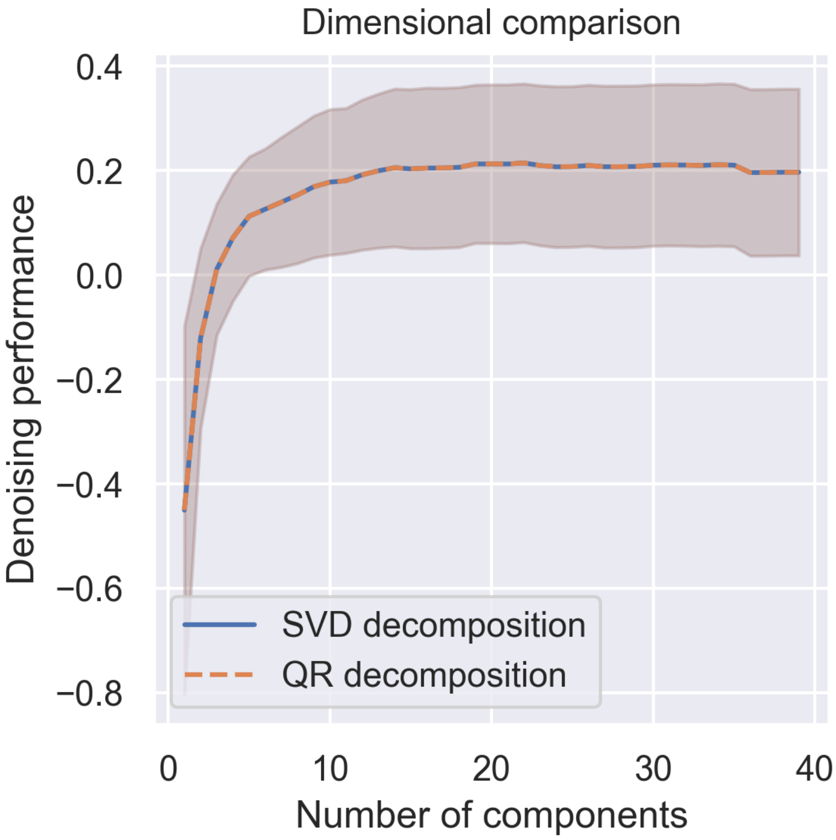

Figure 2.6: Δ as a function of number of dimensions. In blue, the SVD decomposition, in orange the QR decomposition. The two curves are overlapping. The lines represent the mean values of Δ over all the images in the dataset, and the shaded areas represent their standard errors.

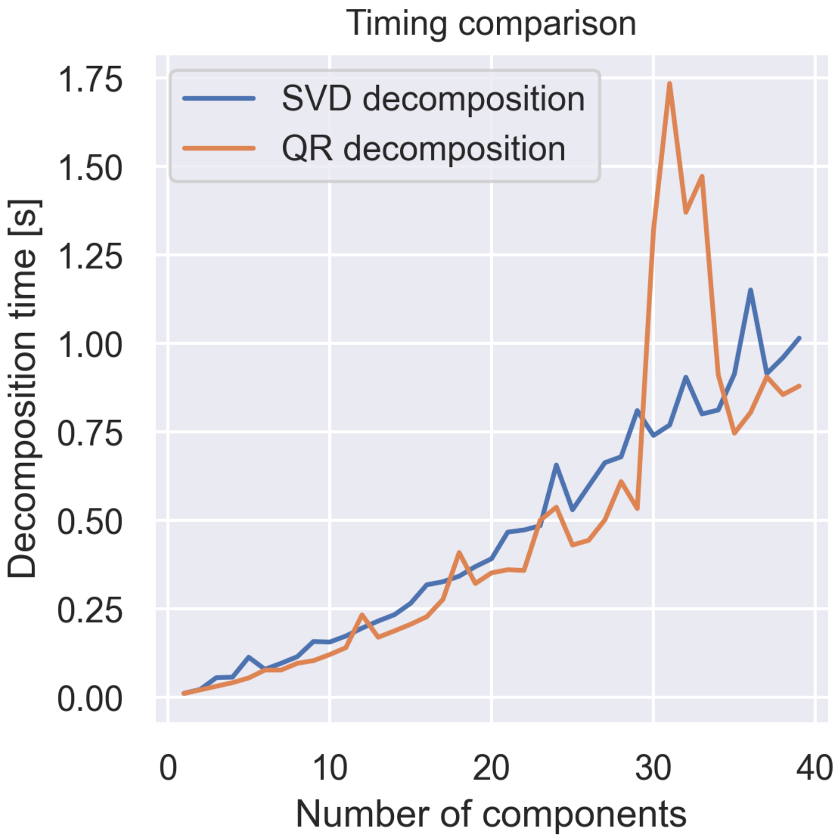

Figure 2.7: Basis computation time as a function of number of dimensions. In blue, the SVD decomposition, in orange the QR decomposition.

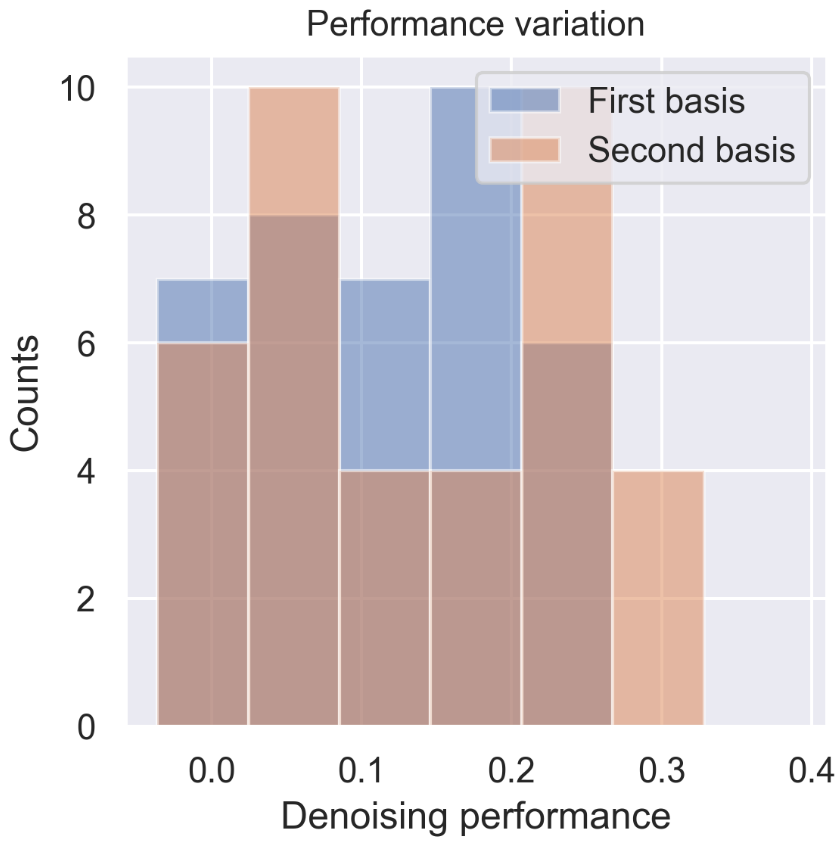

Figure 2.8: Denoising performance calculated with both a basis calculated on old images (“First basis”), and a basis calculated on new images (“Second basis”).

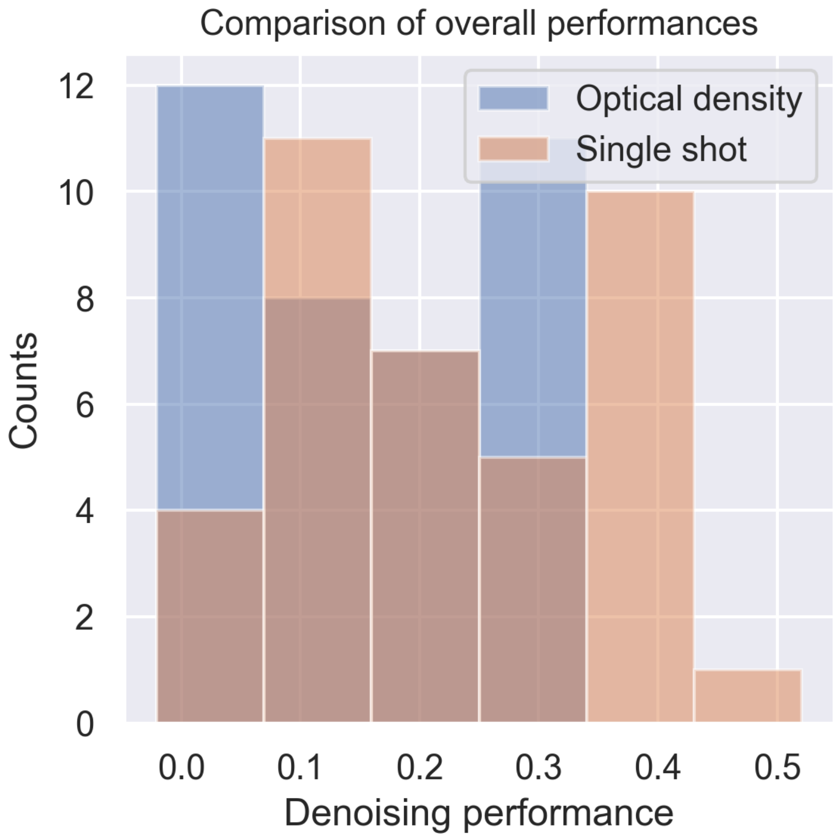

Figure 2.9: Denoising performance of both the optical density method presented in this chapter, and the single shot method similar to the one in [38].

3

Interferometric images analysis

In this chapter, we describe the application of the denoising algorithm to interferometric images. The procedure used to obtain the images is detailed in 3.1, along with an assessment of the background removal procedure. We show the analysis of the interferometric images by fitting an expected profile density in section 3.2, whereas we report the analysis performed using a Fourier transform in section 3.3. We make the final remarks on both the compatibility of the two methods and the comparison with the behaviour of two non interacting condensates in section 3.5.

3.1 Experimental procedure

To prepare the condensate, we have used the apparatus and the procedure described in [46]. The apparatus is capable of producing a two-species Bose-Einstein condensate (BEC) with ^{41}K and ^{87}Rb atoms; however for our images we have only used ^{87}Rb. A scheme of the apparatus is reported in 3.1.

The ^{87}Rb atoms are loaded from a vapour cell into a two-dimensional magneto-optical trap (MOT), where they are pre-cooled and funneled in an atomic beam which is used to load a three-dimensional MOT. Then, the atoms are kept in a compressed MOT stage[1], in which the axial gradient $\partial B_z/\partial z$ of the MOT quadrupole magnetic field is increased from 16 G/cm to 35 G/cm, and in an

---

[1] See [47] for additional details.

optical molasses phase, in which the atoms undergo a damping of their velocity because of an effective viscous force, as the photon scattering is increased when their frequency is Doppler-shifted towards resonance [48]. Afterwards, the atoms are prepared in the $|F = 2, m_F = 2\rangle$ hyperfine state using optical pumping, and subsequently trapped in the magnetic field of the MOT (without the optical fields) with the gradient raised to $\partial B_z/\partial z = 155$ G/cm: the hyperfine state used is selected because it is attracted to a minimum of a magnetic field (*low-field seeking* state). Two far off-resonant laser beams, one stronger and one weaker, that intersect in the centre of the quadrupole field are then turned on.

The next stage is an hybrid evaporative cooling: first, inducing a $|F = 2, m_F = 2\rangle \to |F = 1, m_F = 1\rangle$ transition with a microwave field, the atoms reach a temperature of about $30\,\mu$K; then, the stronger beam is reduced in power, further diminishing the temperature to reach BEC at a temperature of order $0.2\,\mu$K [46].

When only images of the condensate are needed, like in Chap. 2, the trapping fields are then turned off, and the condensate thus expands and falls. After 18 ms, a laser beam resonant with the D_2 transition towards the $5p\,^2P_{3/2}$ electronic excited state takes the absorption image of the BEC.

When we want interferometric images, the additional steps described in the last paragraph of Sec. 1.4.1 are needed. After the condensate is prepared, the zero of the magnetic quadrupole trap is moved in the x direction, exciting a motion of the condensate in the same direction. After the desired Bragg velocity has been reached, all the trapping potentials are turned off, and an optical lattice with wavenumber $k_L = 599$ nm in the x direction applies two resonant $\pi/2$ pulses of $\approx 65\,\mu$s, separated by a time interval Δt_i. The time that passes between the turning off of the trapping fields and this first pulse is called the *delay time*, Δt_d. After Δt_f, the atoms are imaged with absorption imaging (see Sec 2.1); the probe beam propagates along the direction y.

The imaging apparatus is based on a two lens microscope in an *afocal* configuration [16], and can be seen in figure 3.2. In this configuration, the two lenses are situated at a distance $d = f_1 + f_2$, where f_1 and f_2 are the focal distances of, respectively, the first and the second lens, in this configuration the conjugated planes are at infinity. In our case, we have $f_1 = 150$ mm and $f_2 = 500$ mm, giving a magnification $M = f_2/f_1 \approx 3$. The atoms are illuminated from infinity with a laser beam, and are imaged with a CMOS camera (also at infinity). The overall resolution of the system is about $5\,\mu$m. Between the vacuum chamber and the illumination source, there is an iris that can be closed

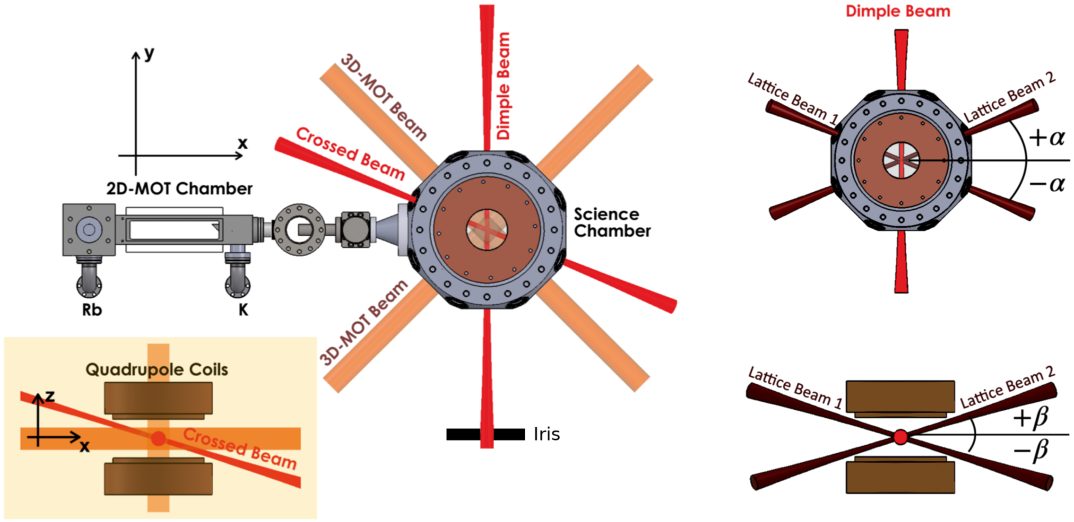

Figure 3.1: Scheme of the experimental apparatus used to obtain the images. On the right are shown the beams used for the preparation of the condensate: the MOT beams and the dimple beam for the optical evaporation, along with the quadrupole coils (inset below) for the generation of the magnetic fields. The probe beam also propagates in the y direction, like the dimple beam; the iris after the science chamber is a field stop for the imaging (imaging camera not shown). On the right we can see the two beams used to create the optical lattice for the Bragg scattering, along with the dimple beam (for reference); the angles α and β are, respectively, of 22.5° and 16°. Using a laser with a wavelength of 1064 nm, we obtain an optical lattice with spacing 599 nm. Image on the left from [46], image on the right from [24].

in order to reduce the size of the illumination beam; this in turn minimizes stray light scattered from the optical system and thus improves the signal to noise ratio of the obtained images.

The images used in the remainder of this chapter have been obtained with a fixed Δt_i of 1 ms, varying Δt_d in the range 0.5 ms–3.0 ms, and adjusting Δt_f accordingly, in order to maintain $\Delta t_d + \Delta t_i + \Delta t_f = t_T = 22\,\text{ms}$. A total of 275 images have been used for the analysis, 207 of which were made with a closed iris in the optical path; the other 68 had the iris open instead.

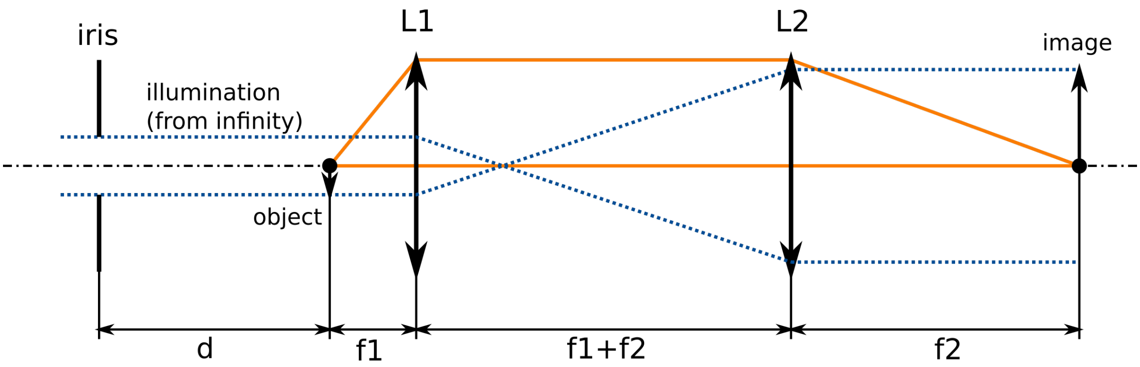

Figure 3.2: Scheme of the imaging apparatus. On the right, at infinity, is situated a laser source for illumination. The light encounters an iris, that reduces the size of the beam and, after a distance $d \approx 40\,\mathrm{cm}$, the atomic cloud, that absorbs a portion of the incoming light. The atoms are contained in a vacuum chamber (not depicted). Then, after a distance $f_1 = 150\,\mathrm{mm}$ is located a lens L_1 whose focal length is equal to f_1. A second lens L_2, of focal length $f_2 = 500\,\mathrm{mm}$ is situated at a distance $f_1 + f_2$. Finally, at a distance f_2 there is a camera which images the atoms. In blue are shown two symmetric rays for the illumination, in orange a marginal ray and the axial ray.

3.1.1 Denoising

We denoised all the images with the algorithm of chapter 2; a basis of 80 images was needed, probably due to the more complex nature of these images. A comparison of a clean and denoised image can be seen in figure 3.3. Before denoising, the images with the closed iris had to be appropriately cropped and padded with zeros, in order to maintain the same image size (a detail that will be important in section 3.3). The closed iris images had a denoising performance $\varDelta = 0.10 \pm 0.03$, while those with an open iris had a $\varDelta = 0.02 \pm 0.02$.[2] We can affirm that, in both cases, the application of the denoising algorithm results in a net improvement of the images.

Prompted by the lacklustre behaviour of the algorithm for the open iris images, we have investigated two variants, in order to improve its performance.

---

[2] Both values of $\varDelta$ are reported as mean, plus or minus the standard deviation. Up to two significant figures, the value in the open iris case is 0.021 ± 0.017, and the minimum value of the distribution is 0.004: as such, even for the worse case, is still positive. The values have been corrected to account for the fact that they have been calculated for images of a different effective size.

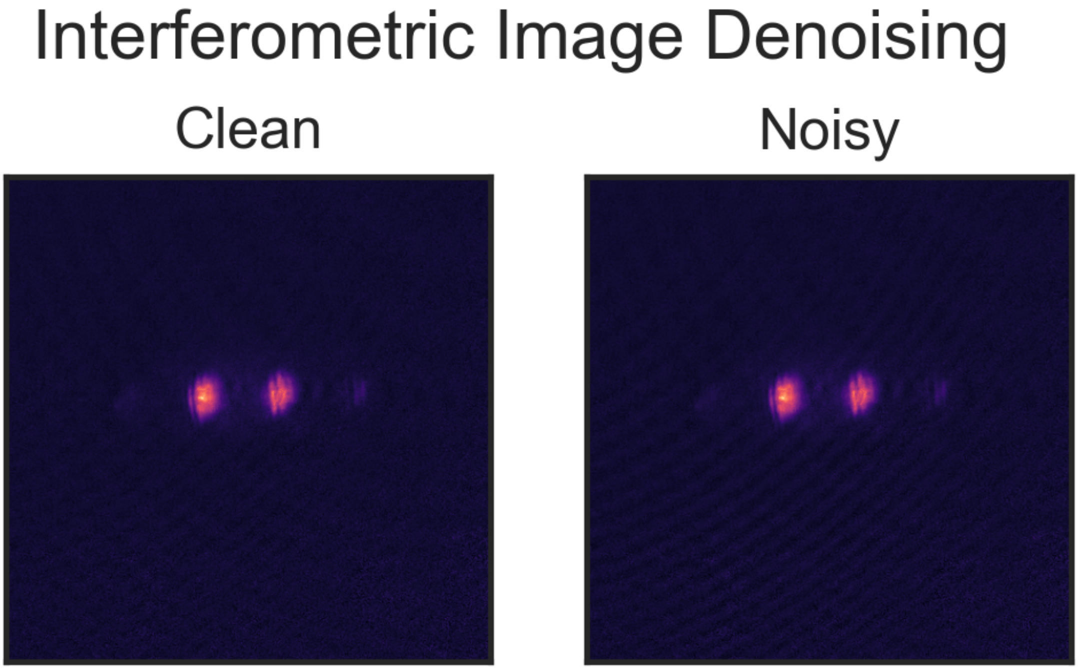

Figure 3.3: Comparison of a clean image with a noisy one in the open iris case, for which the effect of the denoising is more visually evident, albeit less effective when computed with the Δ. The reduction in intensity of the noise pattern is more evident in the zone immediately under the condensates. The condensate on the left is said to be the *left port* of the interferometer, whereas the one on the right is called the *right port*.

In [38], which used a method almost identical to the one we used, the authors explain that they performed the projection on the basis only on an external portion of the image, akin to the *masked image* of (2.2). We performed a test running the algorithm first with the masked projection, and then without, on all the interferometric images; the difference in Δ for the two variants, calculated on the same images, resulted in an identically null distribution. Therefore, the two methods have the exact same performance, up to the precision limit of the machine on which the tests were performed ($\approx 2 \times 10^{-16}$ for 64-bit floating point numbers). The second test ran the denoising procedure not directly on the images, but on the Fourier transform amplitude (the basis images were also transformed before the diagonalization). For the open iris case, we found

$\varDelta = 0.002\,69 \pm 0.000\,04$, whereas for the closed iris $\varDelta = 0.017 \pm 0.003$; [3] the Student's t-test with, respectively, T-Statistics of 8.7 and 40.0, 205 and 66 degrees of freedom, and p-values negligibly different from zero, we can reject the null hypothesis that the $\varDelta$ distributions are the same for the two variants. This also means that the variant of the algorithm that we used until now is the best one, as far as performance is concerned.

The difference in denoising performance with the results in section 2.7 could be due to a different symmetry of the image. The values we found in the aforementioned section used an image of a roughly circular BEC, whereas the images used in this section have only a twofold rotational symmetry axis. Figure 4 of [38] also demonstrates the algorithm with a sixfold rotational symmetry axis. In order to test this claim, some tests could be performed with BEC disposed in shapes of increasingly high rotational symmetry. While conceptually simple, the manipulation of atomic clouds with this kind of precision is not an experimentally trivial proposition.

3.2 Profile fit analysis

One common method for the analysis of interferometric images is the fitting of the density profile of one of the two *ports* of the interferometer. More in detail, the interference image is summed along its vertical axis y, giving a marginal[4] interference pattern as a function of x:

$$n(x) = A_1 e^{\frac{-(x-x_1)^2}{2\sigma_1^2}} + A_2 e^{\frac{-(x-x_2)^2}{2\sigma_2^2}} + c\sqrt{A_1 e^{\frac{-(x-x_1)^2}{2\sigma_1^2}} \cdot A_2 e^{\frac{-(x-x_2)^2}{2\sigma_2^2}}} \cdot \cos\left(kx + \phi\right) + n_0; \tag{3.1}$$

in this equation the densities are supposed gaussian. This approach has several advantages and disadvantages. The main advantage is the plethora of parameters that can be inferred, giving a lot of information about the density distribution; the variable ϕ, which is in many cases the key observable for interferometer experiments, can be determined with this method.

The main disadvantage of the method is also related to the many parameters of (3.1). This often causes a bad fit of the observed density, unless the initial guesses and the lower and upper limits for the parameters are adjusted, which

---

[3] $\varDelta$ reported as mean value, plus or minus the standard deviation.

[4] Used in analogy with the nomenclature for joint and marginal probability distributions.

is an error prone procedure that requires human intervention. In order to make better initial guesses, a two step procedure is used: first, the density profile is fitted with one gaussian curve, which is then used to infer various initial guesses for the images. While this mitigates the needs for adjustments, it does not completely solve the aforementioned problems.

We analyzed the images described in section 3.1 with the fit method. For each image, the wavenumber k and its uncertainty δk, taken as the 1σ confidence interval, was extracted from the fit results. For each Δt_d, we calculated the wavenumber and its uncertainty as the weighted mean and standard deviation, using as weights $1/\delta k^2$. The results of the fit are reported in figure 3.4.

3.3 Fourier transform analysis

If the variable of interest is the wavenumber k of the interference pattern, a method based on Fourier transforms of the images can be used. The images are first transformed using a two dimensional Fourier transform

$$\tilde{n}(k_x, k_y) = \frac{1}{2\pi} \int_{\mathbb{R}^2} \mathrm{d}x\, \mathrm{d}y\; n(x,y) e^{-i(k_x x + k_y y)} \,. \tag{3.2}$$

The Fourier coefficients $\tilde{n}(k_x, k_y)$ are then transformed in polar coordinates, obtaining a phase profile $\arg(\tilde{n})(k_x, k_y)$ and an amplitude profile $|\tilde{n}|(k_x, k_y)$; the amplitude profile can then be used to determine the frequency k_p at which the peaks occur. Then, the phase of the fringes $\phi_p = \arg(\tilde{n})(\mathrm{k}_p)$ can be obtained.

When doing the Fourier transform, some attention must be had that the transform is performed only on one of the ports. Failure to do so will result in additional peaks, with a spacing $\delta k = 2\pi/(x_1 - x_2)$, as can be seen in figure 3.5. An useful trick is to pad with zeros the single-port images, in order to have the coefficients of the fast Fourier transform (FFT) referred to the same frequencies.[5]. If desired, δk could also be used to calculate the separation of the centroids of the two gaussians.

The main advantage of this method is that it does not require the adjustment of parameters, and therefore less intervention of the experimenter. It can also determine the phase of the interferometer fringes, by computing the phase of the image at the frequency corresponding to the peak; a comparison of the

---

[5] Here, we have used the FFT algorithm for all the numerical calculations of Fourier transforms

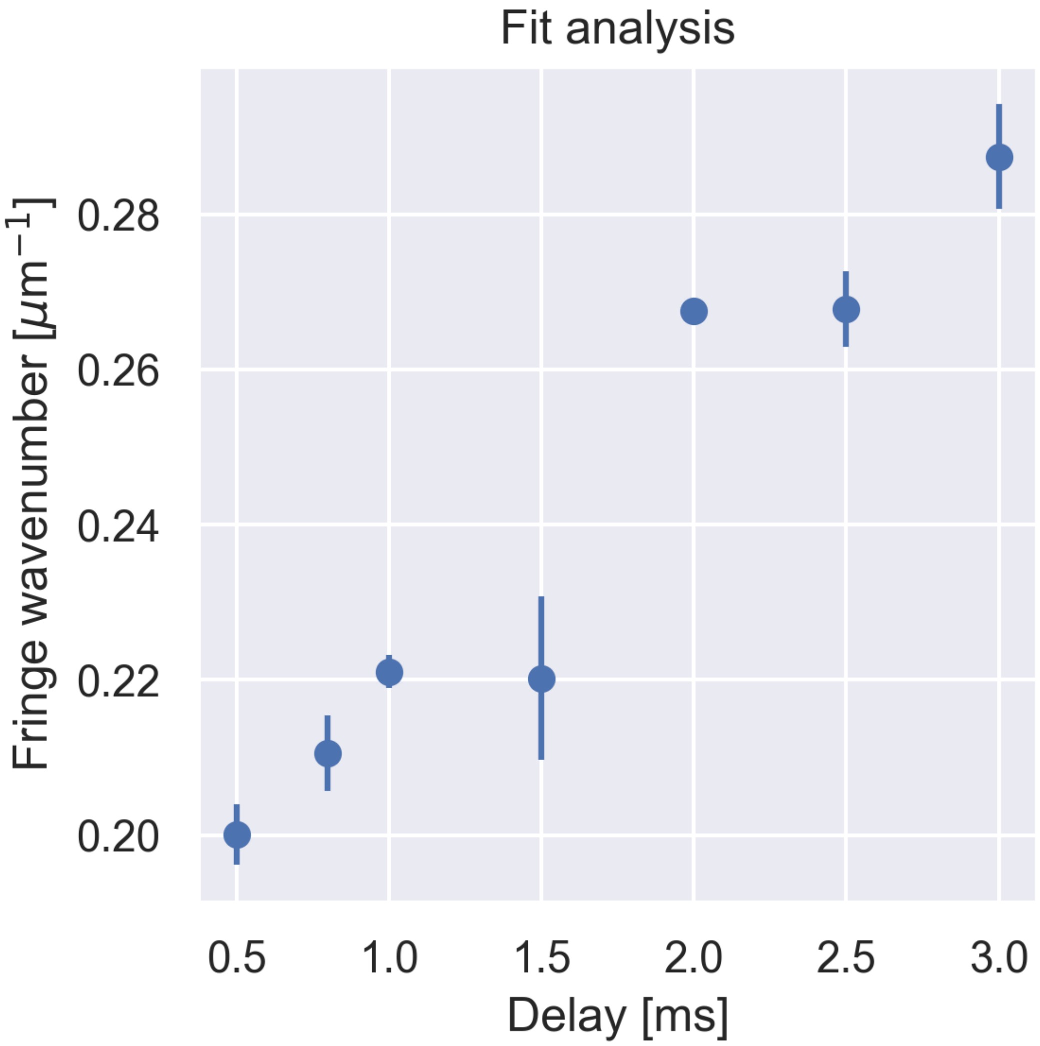

Figure 3.4: Results of the analysis of interferometric images with the fit method. The fringe wavenumber is reported as a function of the delay Δt_d. The mean value and error for each value of Δt_d was calculated as the weighted mean and standard deviation, using as weights the inverse squares of the errors on the fit result. The errors are reported as the 68% confidence intervals on the estimated fit wavenumber.

phase estimation is provided in section 3.5. The disadvantage is that Fourier analysis reveals less information about the distributions in a simple way: while theoretically, the phase and amplitude of $\tilde{n}$ contain the same information as $\tilde{n}$, it would require a bit of effort to extract them. However, if desired, one could calculate the expressions of the parameters by analytically solving the integral in (3.2), having as input an expression for the expected $n(x,y)$. A somewhat simplified expression can be found by integrating along the vertical axis of the image and calculating the transform of (3.1):

$$\begin{aligned}\tilde{n}(k_x) &= \frac{1}{\sqrt{2\pi}}\int_{\mathbb{R}} \mathrm{d}x\, n(x) e^{-ik_x x} \\ &= \sigma_1 A_1 e^{-\frac{k_x^2\sigma_1^2}{2}} + \sigma_2 A_2 e^{-\frac{k_x^2\sigma_2^2}{2}} \\ &+ \frac{c\sqrt{A_1A_2}}{\sqrt{2P}} e^{-\left(R+\frac{k_x^2-Q^2}{4P}\right)} \cos\left(\phi + \frac{k_x Q}{2P}\right) \\ &+ n_0\sqrt{2\pi}\delta(k_x),\end{aligned} \tag{3.3}$$

where k is the same that appears in (3.1), and

$$\begin{cases} P = \dfrac{\sigma_1^2+\sigma_2^2}{4\sigma_1^2\sigma_2^2} \\ Q = -\dfrac{\sigma_2^2 x_1 + \sigma_1^2 x_2}{2\sigma_1^2\sigma_2^2} \\ R = \dfrac{\sigma_2^2 x_1^2 + \sigma_1^2 x_2^2}{4\sigma_1^2\sigma_2^2}. \end{cases}$$

In order to determine its parameters, a fit in two dimensions would be needed, thus negating the advantage of the simpler and faster analysis that uses the Fourier transform. The derivation of (3.3) can be found in appendix B.

3.4 Expected wavenumber

We can make use of what we learned about the wave functions of BEC in Eq. 1.2 to calculate the expected behaviour of the wave number as a function of Δt_d. For a Thomas-Fermi wave function, that for simplicity we will consider in one dimension,

$$n(x,t) = a_0(t) - a_x(t)x^2,$$

where

$$\begin{cases} a_0 = \dfrac{\mu}{g\Lambda(t)} \\ a_x = \dfrac{1}{2g\Lambda(t)} \dfrac{m\omega_x^2(0)}{\lambda_x^2(t)} x^2. \end{cases}$$

If we suppose that our wave function is of the form

$$\phi(x,t) = \sqrt{n(x,t)} e^{iS(x,t)},$$

the probability current density [15]

$$j(x,t) = -\frac{i\hbar}{2m}\left(\phi^*(x,t)\frac{\partial}{\partial x}\phi(x,t) - \phi(x,t)\frac{\partial}{\partial x}\phi^*(x,t)\right),$$

by substituting $j = nv$, tells us that the velocity field is

$$v(x,t) = \frac{\hbar}{m}\frac{\partial}{\partial x}S(x,t),$$

and, using Eq. 1.19, we conclude that the phase is

$$S(x,t) = \frac{m}{2\hbar}\frac{\dot{\lambda}}{\lambda}x^2$$

In our Bragg interferometer, the condensates interfering are the two components with the same momentum that have been obtained with the interferometric sequence. Therefore, for the right arm, supposing that there is a distance d between the centres of the wavefunctions,

$$\begin{cases} S_{1R} = S\left(x - \dfrac{d}{2} + \dfrac{\hbar k_L}{m}t, t\right) = \dfrac{m}{2\hbar}\dfrac{\dot{\lambda}}{\lambda}\left(x - \dfrac{d}{2} + \dfrac{\hbar k_L}{m}t\right)^2 \\ S_{2R} = S\left(x + \dfrac{d}{2} + \dfrac{\hbar k_L}{m}t, t\right) = \dfrac{m}{2\hbar}\dfrac{\dot{\lambda}}{\lambda}\left(x + \dfrac{d}{2} + \dfrac{\hbar k_L}{m}t\right)^2 \end{cases},$$

and we have

$$\Delta S_R(t) = S_{2R} - S_{1R} = \frac{m}{\hbar}\frac{\dot{\lambda}}{\lambda}dx + \frac{\dot{\lambda}}{\lambda}dk_L t;$$

Because $\dot{\lambda}/\lambda \approx 1/t$ for large t [49],

$$k_f = \frac{m}{\hbar}\frac{d}{t}. \tag{3.4}$$

We can now calculate the expected wavenumber k_f for our interferometric images. The parameter $d = |x_1 - x_2|$ has been calculated from the fit analysis in the previous section as $d = (5 \pm 1)$ µm. A linear fit of d as a function of Δt_d indicates a very weak correlation coefficient of R^2 =0.024, therefore there is no significant correlation between the two variables, and taking the mean value is justified. The m in (3.4) is the mass of one ^{87}Rb atom $m(^{87}\text{Rb}) = 1.443 \times 10^{-25}$ kg [41],[6] and the time is the total time of 22 ms, resulting thus in a value of $k_f = (0.31 \pm 0.06)$ µm^{-1}.

3.5 Remarks

We compared the results obtained for k in the two methods. For each image, we subtracted the value k_{fit} found by fitting from the value k_{Fourier} found by Fourier analysis: $\Delta k(i) = k_{\text{fit}}(i) - k_{\text{Fourier}}(i)$, finding a mean value of -7×10^{-4} and a standard deviation of 1×10^{-3}. A one sample Student's t-test, performed against the hypothesis that the mean of the distribution was compatible with 0 found a T-Statistic of −0.26, with 176 degrees of freedom, resulting in a p-value of 0.80. Therefore, we do not reject the null hypothesis. In figure 3.7 we can see the comparison of the two analysis methods for what concerns the estimation of the wavenumber. The two methods provide compatible values for the estimated quantity, but the fitting method is usually more accurate.

Concerning the phase, the values computed with the two methods are reported in figure 3.8. Because, in order to estimate the phase, the wavenumber of the peak has first to be found, we associated to the wavenumber of each peak the set of its two nearest neighbours,[7] and calculate the phase of the points of the set

$$\Phi(k_i) = \{\arg[\tilde{n}(k)]\,|\,k = k_{i-1}, k_i, k_{i+1}\},$$

---

[6] This is because we are considering non interacting, i.e. one particle, states.

[7] The frequencies of a signal transformed with the FFT algorithm are:

$$k_i = \frac{i \cdot k_s}{N},$$

where k_s is the sampling wavenumber, N is the number of points in the signal, and i goes from $-N/2$ to $N/2 - 1$.

where k_i is the $i-$th wavenumber, and we took as the error half the range of $\Phi(f_i)$:

$$\delta(k_i) = \frac{\max \Phi(k_i) - \min \Phi(k_i)}{2}.$$

For the phase estimated with the fit, instead, we have taken as the error half the modulus of the 95% confidence interval. As can be seen in the aforementioned figure, the Fourier method is invariably worse than the fitting method. This is not surprising, as the phase is very chaotic with respect to k, and as such a small uncertainty in k can result in a big uncertainty on ϕ. We conducted a test to asses the compatibility of the two measurements identical to the one done in the previous paragraph, which resulted in a T-Statistic of 0.071, with 125 degrees of freedom, reulting in a p-value of 0.94. Therefore, we cannot reject the null hypothesis that the two measurements of ϕ are compatible.

We can see, from figure 3.7, that the wavenumber of the fringe pattern has a dependence on the delay time Δt_d. From the treatment in section 3.4, there should be no dependence on Δt_d, but only on the total time, which was instead kept constant for every run of the experimental sequence. Therefore, there is no qualitative agreement with the theory for the non interacting condensates. A quantitative analysis has also been made with a one sample Student's t-test for each set of measures obtained with the same Δt_d; the p-values found were negligibly different from zero, with the highest value found of 3.7×10^{-6} for the k obtained with the fitting method for $\Delta t_d = 3.0\,\mathrm{ms}$.

Therefore, the wave number of the interferometric fringes we have found in this chapter are not compatible with the expected values for the non interacting case, independently confirming the results in [24]. Varying the delay time Δt_d, we change the condensate density when the interferometric sequence is started. From this, we conclude that the wavenumber shift is due to the interatomic interactions. This is confirmed by the analysis done with Gross-Pitaevskii simulations in [24].

From Fig. 3.9, we can see that, with good approximation, the difference between the wavenumbers found experimentally k and the theoretical wavenumber for the ideal case k_i can be approximated as

$$\Delta k(t) = k_i - k(t) = A + B\Delta t_d.$$

A linear fit performed with this model results in a R^2 of 0.96, indicating a good correlation between the variables. For the parameters, we find that $A = 0.126\,\mu\mathrm{m}^{-1}$ (95% CI: $0.122\,\mu\mathrm{m}^{-1}$–$0.140\,\mu\mathrm{m}^{-1}$), and $B = -34\,\mu\mathrm{m}^{-1}/\mathrm{s}$ (95%

CI: $-42\,\mu\mathrm{m}^{-1}/\mathrm{s}$–$-26\,\mu\mathrm{m}^{-1}/\mathrm{s}$). For longer Δt_d, we expect deviations from the linear behaviour as $\Delta k \to 0$ as $\Delta t_d \to +\infty$, since the density decreases with Δt_d and the condensate tends to an ideal condensate with negligible interactions.

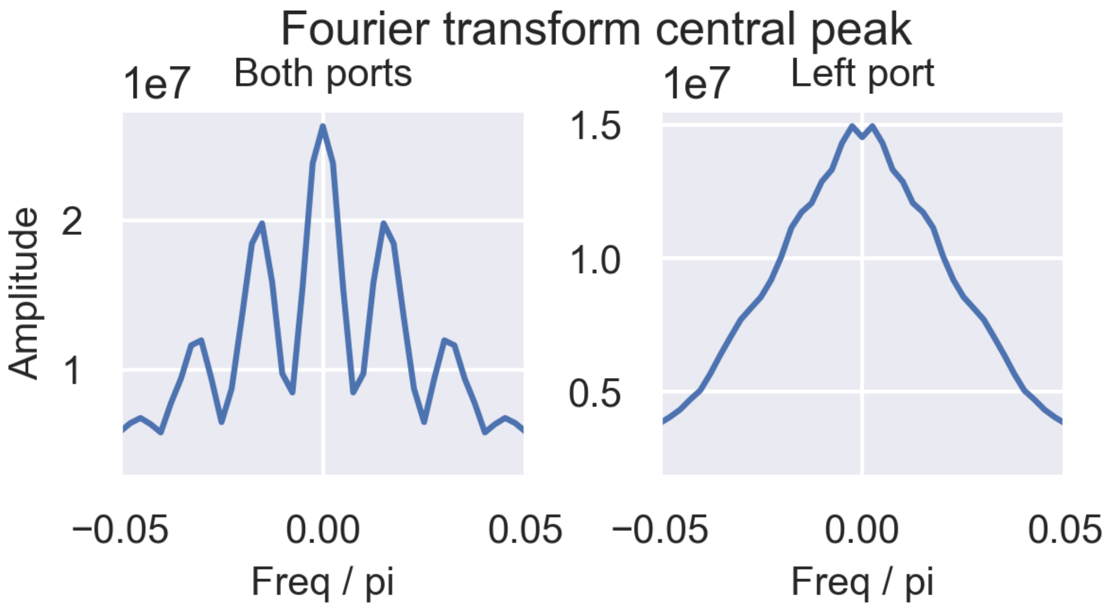

Figure 3.5: Central peak of the Fourier transform made on both ports of the interferometer (left), and only on the left port (right). In order to have the same frequencies in the FFT, the left port image has been adequately padded with zeros.

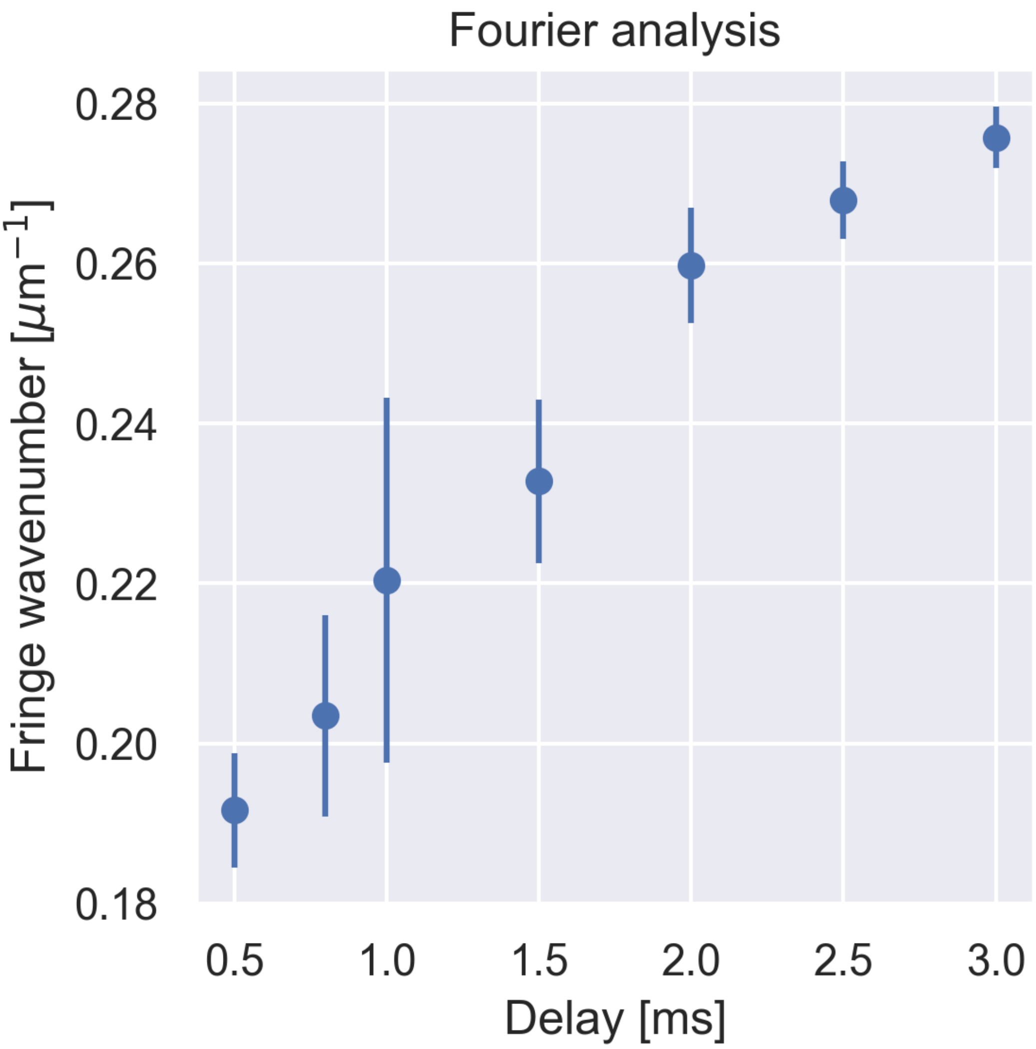

Figure 3.6: Results of the analysis of interferometric images with the Fourier method. The fringe wavenumber is reported as a function of the delay Δt_d. The errors on the experimental points are reported as the standard deviations of the measured wavenumbers.

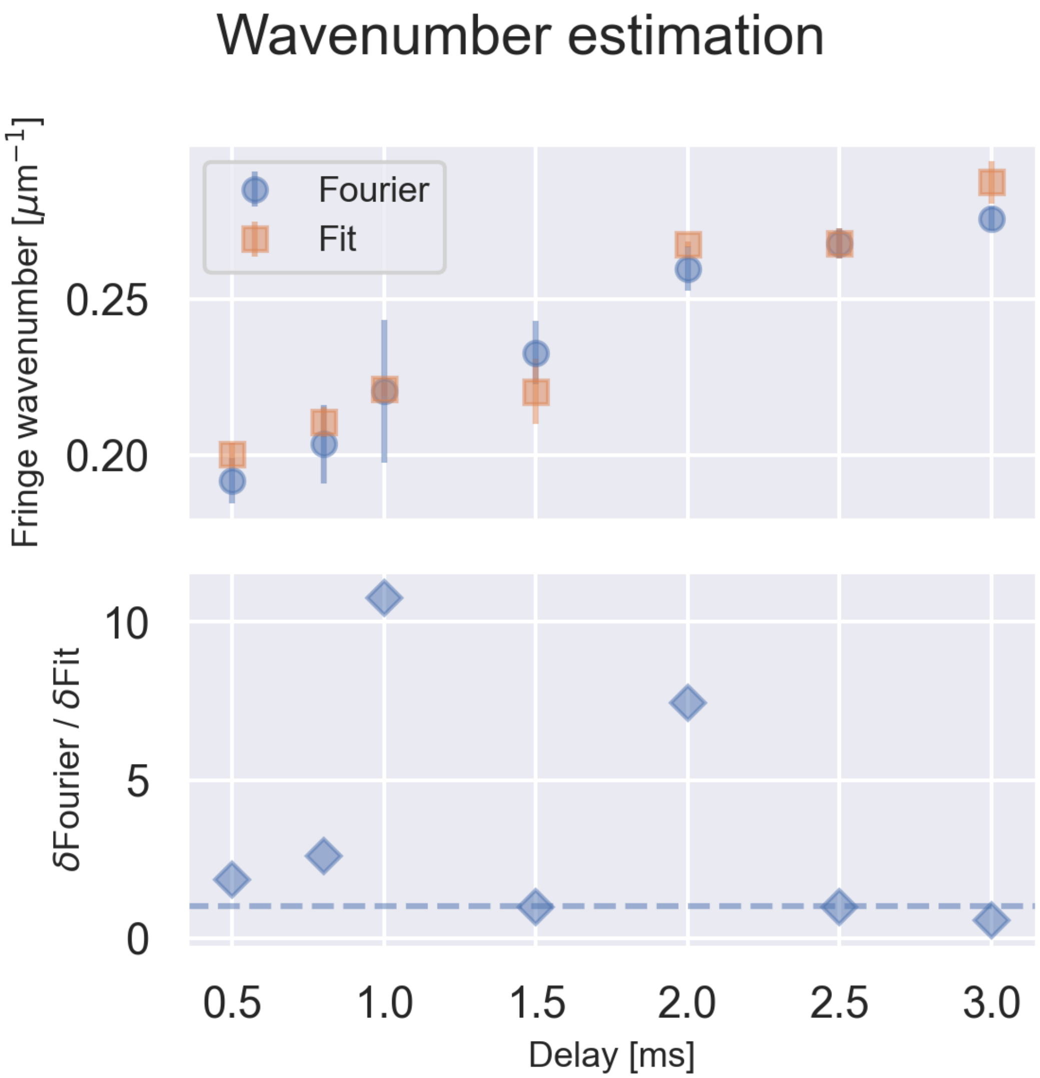

Figure 3.7: Comparison of the two methods of analysis with respect to k determination. Above are reported the found values of the wavenumber and their errors as a function of Δt_d. The means and errors have been calculated as in figures 3.4 and 3.6. We found that the estimated values for the same Δt_d are compatible for the two methods. Below, we can see the error ratio as a function of Δt_d (which is the parameter under experimental control), where the δFourier and the δFit are the same errors of the graph above. The dashed line marks the δFourier/δFit$=1$ level.

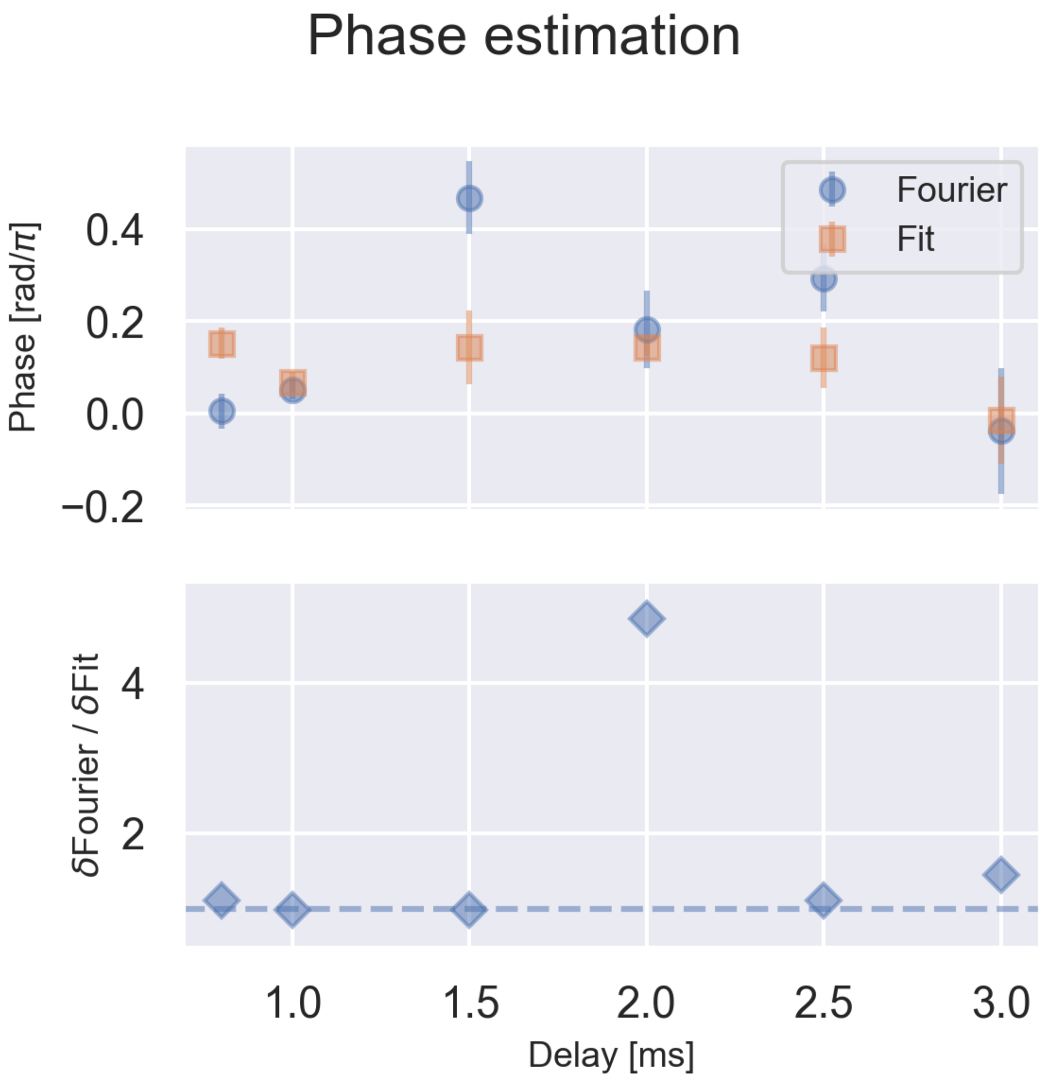

Figure 3.8: Comparison of the two methods for the estimation of the phase. Above are reported the found values of the phase and their errors as a function of Δt_d. The means and errors have been calculated with the weighted mean and associated error, for each method, of the estimated phases corresponding to the same Δt_d. The values estimated with the two methods are not compatible. Below, we can see the error ratio as a function of Δt_d (which is the parameter under experimental control), where the δFourier and the δFit are the same errors of the graph above. The dashed line marks the δFourier/δFit= 1 level. The Fourier method is substantially worse in every case.

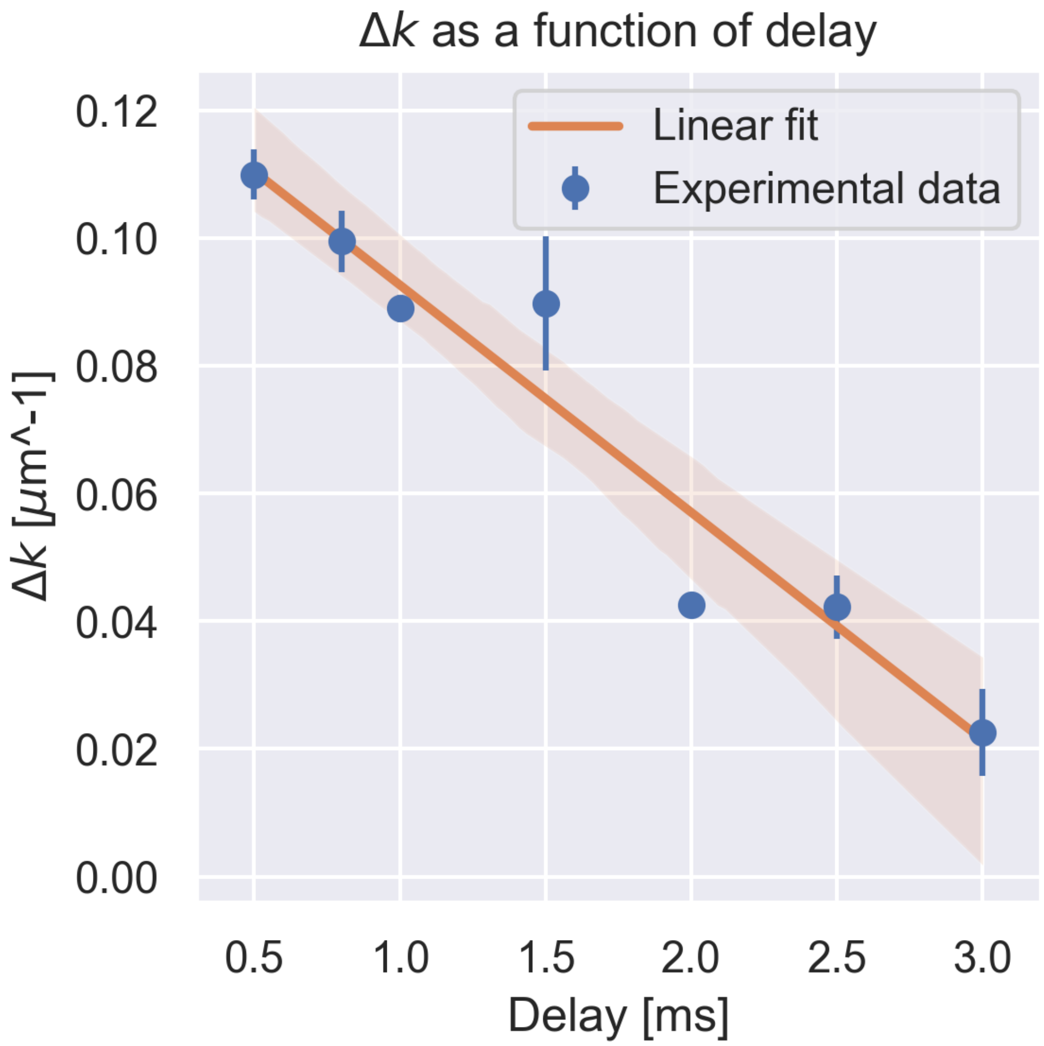

Figure 3.9: Fit of Δk as a function of the delay time. In blue the experimental points; the error bars represent the 95% confidence interval obtained from the fit parameters. In orange, the fitted linear relation $\Delta k = A + B\Delta t_d$; the shaded area represents the 95% confindence interval on the fit. The fit is good, with an R^2 =0.96, but we expect deviations from linearity for longer Δt_d.

4

Conclusions and future developments

4.1 Denoising algorithm

The denoising algorithm developed in chapter 2 has been found to work adequately for images of condensates, but its performance is lacking when applied to interferometric images.

The algorithm has been optimized with respect to three parameters: the basis dimension, the kind of decomposition and the utilization of optical density or raw images, with the target of having both a quick computation time and the best possible denoising. For images of a BEC, this means using the SVD decomposition on a basis of 30–40 raw images; on the reconstructed noise pattern then we shall calculate the optical density.

The best denoising performance was found for the single-shot algorithm for an image of a spherically symmetric BEC, and its value, as reported in section 2.7, is of $\mathit{\Delta} = 0.21 \pm 0.12$. On the contrary, for interferometric images the algorithm is of limited utility when combined with a closed iris that removes part of the starting noise, when it results in a fraction of 0.10 ± 0.03 of the noise being removed; its usefulness without an iris is almost insignificant, with the fraction of removed noise equal to 0.02 ± 0.02.

The difference in denoising performance with the results in section 2.7 could be due to a different symmetry of the image. The values we found in the

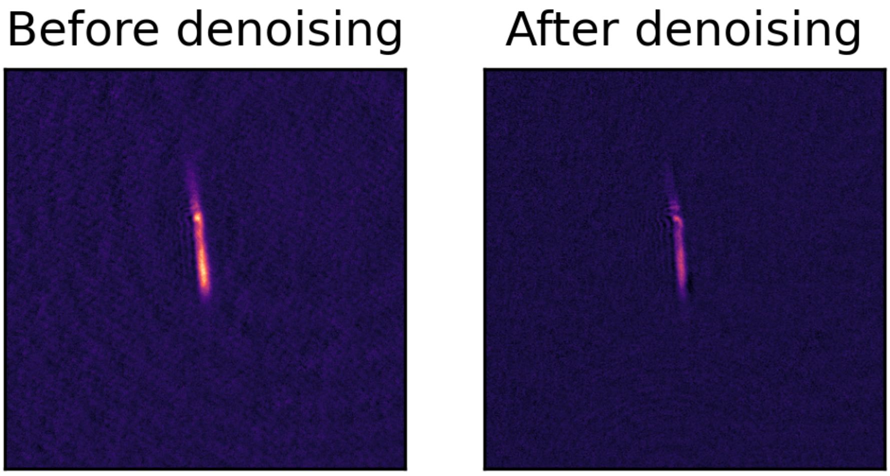

Figure 4.1: Image of an elongated condensate used to investigate why the performance of the denoising algorithm is significantly lower for an interferometric image. While this image has been chosen because the effect of the denoising is clearly visible, the distribution of the denoising performance is compatible with that of the interferometric images. The proposed motivation for this is that the algorithm acts poorly with objects with low rotational symmetry.

aforementioned section used an image of a roughly circular BEC, whereas the images used in this section have only a twofold rotational symmetry axis. Figure 4 of [38] also demonstrates the algorithm with a sixfold rotational symmetry axis. In order to test this claim, we made a denoising test with images of elongated condensates, such as that in figure 4.1. We obtained a denoising performance of 0.10 ± 0.20. While the standard deviation of Δ for this tests is unusually high, we can see a similar value to what was obtained for the fringes. A Student's t-test, with the null hypothesis that the distributions for the elongated condensates and the fringes are compatible, results in a T-Statistic of 0.095, with 279 degrees of freedom, and the p-value is thus 0.92.

We can thus conclude that images with a low degree of rotational symmetry are not well suited for denoising with our algorithm.

The natural development of this thesis would be of implement an automatic image processing pipeline for the K-Rb experiment at LENS, where our algorithm would be used to process absorption images as soon as they are captured. This has not been possible yet because of the recent worldwide events.

Another development of the work done on our algorithm would be to investigate whether it is indeed possible to mitigate the detrimental effect of the low symmetry on the denoising performance. While some simple variants have already been tried without success in 3.1.1, it cannot be excluded that other variants would not achieve this goal.

Moreover, it would be interesting to combine our algorithm with one based on a neural net, such as that in [39]. While the design and implementation of such an algorithm would be quite difficult and time consuming, because both of its state-of-the-art nature and the necessity of acquiring thousands of images, a carefully devised hybrid noise removal scheme could offer unprecedented capabilities for improving the imaging precision in cold atoms experiments.

4.2 Interferometric analysis

The analysis of the interferometric images was done with two methods, one based on fitting an expected density profile and the other based on the Fourier transform of the image. The first of the two methods is superior, both in the precision of the estimation of experimental quantities for most situation, and in number of parameters that can be simply extracted from the images. The only advantage of the second method is that it is less time consuming to extract the wavenumber of the interferometric fringes, and, for more tightly spaced fringes, can be equally or slightly more precise than the fitting method.

The wavenumber of the interferometric fringes is not compatible both qualitatively and quantitatively with the expected wavenumber for the non interacting case. This conclusion, confirming what was found in [24], is of paramount importance for atom interferometry with ^{87}Rb BEC. This isotope is of current use in many atomic experiments, with some of the most recent being [50], [51], [52], [53], and therefore understanding the role of the interactions in the evolution of the phase can have a twofold interest. First, it could advance the field of precision measurements by enabling to compensate for unwanted effects due to interactions in the condensate; second, the study of the evolution of the phase in an interacting condensate can be of particular interest to further our knowledge of quantum many-body physics.

A

Code for the denoising algorithm

The code used for this thesis is all written in the Python programming language, version 3.6.9, and using the Numpy library, version 1.16.6, for computation purposes.[1] Here are reported the main functions used in the denoising programs.

A.1 The `calcBasis` function.

This function calculates a noise basis from a list of images. Every element of the `images` list must be a `numpy.ndarray` array. It returns a list of arrays, each of those representing a vector of the decomposed space (see 2.2). The `normalize` function return a list of normalized vectors.

```python
import numpy as np

def calcBasis(images):
  images = normalize(images)
  imageArray = np.array([x.flatten() for x in images]).transpose()
  q, *__ = np.linalg.svd(image_array, full_matrices = False)
  return [vec.flatten() / np.linalg.norm(vec)
          for vec in np.hsplit(q, q.shape[1])]
```

---

[1] For further details, see `https://python.org`, `https://numpy.org`.

A.2 The `cleanImage` function

This function calculates the clean image, from an optical density image with the background still present, `image`, and a basis list as returned by `calcBasis`

```
import numpy as np

def cleanImage(image, basis):
  weights = [vect.dot(image.flatten()) for vect in basis]
  noise = sum([weight * vect.reshape(image.shape)
               for weight, vect in zip(weights, basis)])
  return image - noise
```

A.3 The `denPerf` function

This function calculates the denoising performance. It takes as inputs an image `noisy` before the denoising, the same image after the denoising `clean`, and the mask `imageMask`, an array which is 1 in a region where the atoms are contained and 0 outside. The `np.ma.array` class is a numpy class for a *masked* array, which is composed of a numeric array and a logical mask. All the elements of the array, for which the corresponding entry in the mask is `True`-like, are considered masked and are skipped during all the computations. In this way, we can have a simple and correct way of excluding a portion of the image from the calculation of the denoising performance.[2]

```
import numpy as np

def denPerf(noisy, clean, imageMask):
  myNoisy = np.ma.array(noisy, mask=imageMask)
  myClean = np.ma.array(clean, mask=imageMask)
  return myNoisy.std() - myClean.std()
```

A.4 Usage example

Suppose, for example, that we have to perform our denoising on a series of images of condensate clouds and images of backgrounds called, respectively,

---

[2] Multiplying the image by a mask composed of zeros in the excluded region and ones in the preserved region is a simple solution, however it is incorrect, as the so obtained denoising performance is a function of the offset of the image.

`bec-x.fmt` and `backg-x.fmt`, where `x` is a number and `.fmt` a suitable format.[3] We suppose also that we have a `readImg` function, that reads an image as a numpy matrix given its filename, and a `saveImg` that saves it. Then, we could use our denoising functions in the following way:

```python
import numpy as np

# function definitions

# we have a list becFilenames of filenames of images we want to
# denoise and an analogous list backgFilenames for the
# backgrounds we want to use

backgs = [readImg(x) for x in backgFilenames]
noiseBasis = calcBasis(backgs)

for imgName in becFilenames:
  noisy = readImg(imgName)
  clean, _ = cleanImage(noisy, noiseBasis)
  saveImg(clean, ``clean'' + imgName)
```

---

[3] Usual formats used for this images are the Flexible Image Transfer System `.fits` format and the ImageCore `.sis` format.

B

Calculation of the Fourier transform of the fitting function

The expected marginal density for two interfering condensates (3.1) is:

$$n(x) = A_1 e^{-\frac{(x-x_1)^2}{2\sigma_1^2}} + A_2 e^{-\frac{(x-x_2)^2}{2\sigma_2^2}} + c\sqrt{A_1 e^{-\frac{(x-x_1)^2}{2\sigma_1^2}} \cdot A_2 e^{-\frac{(x-x_2)^2}{2\sigma_2^2}}} \cdot \cos\left(k'x + \phi\right) + n_0.$$

Its Fourier transform is:

$$\begin{aligned}
\tilde{n}(k) = & \frac{1}{\sqrt{2\pi}} \int \mathrm{d}x A_1 e^{-\frac{(x-x_1)^2}{2\sigma_1^2}} e^{-ikx} \\
& + \frac{1}{\sqrt{2\pi}} \int \mathrm{d}x A_2 e^{-\frac{(x-x_2)^2}{2\sigma_2^2}} e^{-ikx} \\
& + \frac{1}{\sqrt{2\pi}} \int \mathrm{d}x\, c\sqrt{A_1 e^{-\frac{(x-x_1)^2}{2\sigma_1^2}} \cdot A_2 e^{-\frac{(x-x_2)^2}{2\sigma_2^2}}} \cdot \cos\left(k'x + \phi\right) \cdot e^{-ikx} \\
& + n_0 \sqrt{2\pi}\, \delta(k).
\end{aligned}$$

All the integrals in this appendix are understood to be integrals on the whole real line. The transforms of the first two terms are

$$\begin{aligned} I_{1,2} &= \frac{1}{\sqrt{2\pi}} \int \mathrm{d}x A_{1,2} e^{-\frac{(x-x_{1,2})^2}{2\sigma_{1,2}^2}} e^{-ikx} \\ &= \sigma_{1,2} A_{1,2} e^{\frac{k^2\sigma_{1,2}^2}{2}}. \end{aligned}$$

The transform of the third term is a bit more complicated:

$$I_3 = c\sqrt{\frac{A_1A_2}{2\pi}} \int \mathrm{d}x \, \exp\left[-\frac{(x-x_1)^2}{2\sigma_1^2} - \frac{(x-x_2)^2}{2\sigma_2^2}\right] \cos\left(k'x+\phi\right).$$

We can separate it in two integrals by substituting

$$\cos\left(k'x+\phi\right) = \frac{1}{2}\left(e^{i(k'x+\phi)} + e^{-i(k'x+\phi)}\right),$$

obtaining

$$I_\pm = c\sqrt{\frac{A_1A_2}{2\pi}} \frac{e^{\pm i\phi}}{2} \int \mathrm{d}x \exp\left[-\frac{1}{2}\left(\frac{(x-x_1)^2}{2\sigma_1^2} + \frac{(x-x_2)^2}{2\sigma_2^2}\right)\right] e^{-i(k\mp k')x}.$$

The convolution theorem [54] states that, for suitable f_1 and f_2,[1] we have

$$\mathscr{F}[f_1 \star f_2] = \sqrt{2\pi}\mathscr{F}[f_1] \cdot \mathscr{F}[f_1],$$

and

$$\mathscr{F}[f_1 \cdot f_2] = \frac{1}{\sqrt{2\pi}}\mathscr{F}[f_1] \star \mathscr{F}[f_2],$$

where $\mathscr{F}$ is the map that associates transform, and $\star$ is the convolution product

$$f \star g = \int f(x)g(x-\chi)\mathrm{d}\chi.$$

In I_+ we identify

$$\begin{cases} f_1 = \exp\left[-\frac{1}{2}\left(\frac{(x-x_1)^2}{2\sigma_1^2} + \frac{(x-x_2)^2}{2\sigma_2^2}\right)\right], \\ f_2 = e^{ik'x} \end{cases}$$

---

[1] Namely, their Fourier transform shall exist.

and, because $\mathscr{F}[f_2](k) = \sqrt{2\pi}\delta(k' - k)$,

$$I_+ = \frac{1}{\sqrt{2\pi}}\mathscr{F}[f_1](k) \star \mathscr{F}[f_2](k) = F[f_1](k').$$

The problem now consists of calculating $F[f_1](k')$.

We can see that the argument of f_1 is

$$\begin{aligned}
&-\frac{1}{2}\left(\frac{(x-x_1)^2}{2\sigma_1^2} + \frac{(x-x_2)^2}{2\sigma_2^2}\right) \\
&= -\frac{\sigma_2^2(x-x_1)^2 + \sigma_1^2(x-x_2)^2}{4\sigma_1^2\sigma_2^2} \\
&= -\left(Px^2 + Qx + R\right),
\end{aligned}$$

where

$$\begin{cases}
P = \dfrac{\sigma_1^2 + \sigma_2^2}{4\sigma_1^2\sigma_2^2} \\
Q = -\dfrac{\sigma_2^2 x_1 + \sigma_1^2 x_2}{2\sigma_1^2\sigma_2^2} \\
R = \dfrac{\sigma_2^2 x_1^2 + \sigma_1^2 x_2^2}{4\sigma_1^2\sigma_2^2}.
\end{cases}$$

The Fourier transform of f_1 then becomes

$$\begin{aligned}
\mathscr{F}[f_1](k) &= \frac{1}{\sqrt{2\pi}}\int \mathrm{d}x\, e^{-\left(Px^2+Qx+R\right)}e^{-ikx} \\
&= \frac{e^{-R}}{\sqrt{2P}}e^{\frac{(Q+ik)^2}{4P}} \qquad = \frac{e^{-R}}{\sqrt{2P}}e^{-\frac{k^2-Q^2-2ikQ}{4P}}.
\end{aligned}$$

So,

$$\begin{aligned}
I_+ &= \frac{c\sqrt{A_1A_2}e^{i\phi}}{2}\mathscr{F}[f_1](k') \\
&= \frac{c\sqrt{A_1A_2}}{2\sqrt{2P}}e^{-\left(R+\frac{k^2-Q^2}{4P}\right)}e^{i\left(\phi+\frac{kQ}{2P}\right)} \\
I_- &= (I_+)*
\end{aligned}$$

and

$$\begin{aligned} I_3 &= I_+ + I_- \\ &= \frac{c\sqrt{A_1 A_2}}{\sqrt{2P}} e^{-\left(R+\frac{k^2-Q^2}{4P}\right)} \cos\left(\phi + \frac{kQ}{2P}\right) \end{aligned}$$

obtaining thus Eq. (3.3).

Bibliography

1. Cronin, A. D., Schmiedmayer, J. & Pritchard, D. E. Optics and interferometry with atoms and molecules. *Reviews of Modern Physics* **81,** 1051 (2009).
2. Steck, D. A. *Quantum and Atom Optics* `http://steck.us/teaching`.
3. Cohen-Tannoudji, C. *Interferometrie atomique* Notes for the *Course de Physique Atomique et Molecolaire* at the *College de France* for the year 1992-93. `http://www.phys.ens.fr/~cct/college-de-france/`.
4. Cohen-Tannoudji, C. *Interferometrie atomique (suite)* Notes for the *Course de Physique Atomique et Molecolaire* at the *College de France* for the year 1993-94. `http://www.phys.ens.fr/~cct/college-de-france/`.
5. Champenois, C. *et al.* Atomic diffraction by a laser standing wave: Analysis using Bloch states. *European Physical Journal D* **13,** 271 (2001).
6. Svelto, O. & Hanna, D. C. *Principles of lasers* (Springer, 2010).
7. Kapitza, P. L. & Dirac, P. A. The reflection of electrons from standing light waves. *Mathematical Proceedings of the Cambridge Philosophical Society* **29,** 297 (1933).
8. Gupta, S., Leanhardt, A. E., Cronin, A. D. & Pritchard, D. E. Coherent manipulation of atoms with standing light waves. *Comptes Rendus de l'Academie des Sciences - Series IV: Physics, Astrophysics* **2,** 479 (2001).
9. Grimm, R., Weidemüller, M. & Ovchinnikov, Y. B. Optical Dipole Traps for Neutral Atoms. *Advances in Atomic, Molecular and Optical Physics* **42,** 95 (2000).
10. Pitaevskii, L. & Stringari, S. *Bose-Einstein Condensation* 1st ed. (Oxford University Press, 2003).

11. Pethick, C. J. & Smith, H. *Bose–Einstein Condensation in Dilute Gases* 2nd ed. (Cambridge University Press, 2008).
12. Leggett, A. J. Bose-Einstein condensation in the alkali gases: Some fundamental concepts. *Reviews of Modern Physics* **73,** 307 (2001).
13. Castin, Y. & Dum, R. Bose-einstein condensates in time dependent traps. *Physical Review Letters* **77,** 5315 (1996).
14. Storey, P. & Cohen-Tannoudji, C. The Feynman path integral approach to atomic interferometry. *Journal de Physique II* **4,** 75 (1994).
15. Sakurai, J. J. & Napolitano, J. J. *Modern quantum mechanics* 2nd ed. (Pearson Education, 2014).
16. Hecht, E. *Optics* 5th ed. (Pearson Education, 2017).
17. Born, M. & Wolf, E. *Principles of optics: electromagnetic theory of propagation, interference and diffraction of light* 7th ed. (Cambridge University Press, 1999).
18. Zienkiewics, H. K. On the Formation of White-light Fringes in a Mach-Zehnder interferometer. *Aeronautical Research Counsil Reports and Memoranda* **3534,** 1 (1964).
19. Keith, D. W., Ekstrom, C. R., Turchette, Q. A. & Pritchard, D. E. An interferometer for atoms. *Physical review letters* **66,** 2693 (1991).
20. Ramsey, N. F. A Molecular Beam Resonance Method with Separated Oscillating Fields. *Physical Review* **78,** 695 (1950).
21. *The International System of Units* (Bureau International des Poids et Mesures, 2019).
22. Hagley, E. W. *et al.* Measurement of the coherence of a bose-einstein condensate. *Physical Review Letters* **83,** 3112 (1999).
23. Simsarian, J. E. *et al.* Imaging the phase of an evolving Bose-Einstein condensate wave function. *Physical Review Letters* **85,** 2040 (2000).
24. Burchianti, A. *et al. Effect of interactions in the interference pattern of Bose Einstein condensates* arXiv: `2009.01900`.
25. Zhang, Q. *et al.* Precision measurements with cold atoms and trapped ions. *Chinese Physics B* **29,** 093203 (2020).
26. Geiger, R., Landragin, A., Merlet, S. & Santos, F. P. D. *High-accuracy inertial measurements with cold-atom sensors* arXiv: `2003.12516`.

27. Kasevich, M. & Chu, S. Atomic interferometry using stimulated Raman transitions. *Physical Review Letters* **67,** 181 (1991).
28. Hu, Z.-K. *et al.* Demonstration of an ultrahigh-sensitivity atom-interferometry absolute gravimeter. *Physical Review A* **88,** 043610 (2013).
29. Riehle, F., Kisters, T., Witte, A., Helmcke, J. & Bordé, C. J. Optical Ramsey spectroscopy in a rotating frame: Sagnac effect in a matter-wave interferometer. *Physical Review Letters* **67,** 177 (1991).
30. Rosi, G., Sorrentino, F., Cacciapuoti, L., Prevedelli, M. & Tino, G. Precision measurement of the Newtonian gravitational constant using cold atoms. *Nature* **510,** 518 (2014).
31. Asenbaum, P., Overstreet, C., Kim, M., Curti, J. & Kasevich, M. A. *Atom-interferometric test of the equivalence principle at the* 10^{-12} *level* arXiv: `2005.11624`.
32. Mhaskar, R., Knappe, S. & Kitching, J. A low-power, high-sensitivity micromachined optical magnetometer. *Applied Physics Letters* **101,** 241105 (2012).
33. Kominis, I., Kornack, T., Allred, J. & Romalis, M. V. A subfemtotesla multichannel atomic magnetometer. *Nature* **422,** 596 (2003).
34. Jefferts, S. R. *et al.* Accuracy evaluation of NIST-F1. *Metrologia* **39,** 321 (2002).
35. Marti, G. E. *et al.* Imaging Optical Frequencies with 100 μhz Precision and 1.1 μ m Resolution. *Physical Review Letters* **120,** 103201 (2018).
36. Li, X., Ke, M., Yan, B. & Wang, Y. Reduction of interference fringes in absorption imaging of cold atom cloud using eigenface method. *Chinese Optics Letters* **5,** 128 (2007).
37. Ockeloen, C. F., Tauschinsky, A. F., Spreeuw, R. J. & Whitlock, S. Detection of small atom numbers through image processing. *Physical Review A - Atomic, Molecular, and Optical Physics* **82,** 1 (2010).
38. Niu, L. *et al.* Optimized fringe removal algorithm for absorption images. *Applied Physics Letters* **113** (2018).
39. Ness, G., Vainbaum, A., Shkedrov, C., Florshaim, Y. & Sagi, Y. *Single-exposure absorption imaging of ultracold atoms using deep learning* Preprint. arXiv: `2003.01643`.

40. Ketterle, W., Durfee, S. & Stamper-Kurn, D. M. *Making, probing and understanding Bose-Einstein condensates* in *Bose–Einstein Condensation in Atomic Gases* (eds Inguscio, M., Stringari, S. & Weiman, C. E.) (IOP Publishing, 1999), 67.
41. Steck, D. A. *Rubidium 87 D line data* `http://steck.us/alkalidata`.
42. Higham, N. J. *et al. Princeton companion to applied mathematics* (Princeton University Press, 2015).
43. Eckart, C. & Young, G. The approximation of one matrix by another of lower rank. *Psychometrika* **1,** 211 (1936).
44. Markovsky, I. Structured low-rank approximation and its applications. *Automatica* **44,** 891 (2008).
45. Unna, J. B. *Picture of Michelangelo's David* Published under Creative Commons Attribution 3.0 License. Image cropped from original. `https://commons.wikimedia.org/wiki/File:%27David%27_by_Michelangelo_JBU0001.JPG`.
46. Burchianti, A. *et al.* Dual-species Bose-Einstein condensate of K 41 and Rb 87 in a hybrid trap. *Physical Review A* **98,** 1 (2018).
47. Kishimoto, T. *et al.* Direct evaporative cooling of K 41 into a Bose-Einstein condensate. *Physical Review A* **79,** 031602 (2009).
48. Lett, P. D. *et al.* Optical molasses. *Journal of the Optical Society of America B* **6,** 2084 (1989).
49. Dalfovo, F., Giorgini, S., Pitaevskii, L. P. & Stringari, S. Theory of Bose-Einstein condensation in trapped gases. *Reviews of Modern Physics* **71,** 463 (1999).
50. Overstreet, C., Asenbaum, P., Kim, M. & Kasevich, M. Atom-interferometric test of the equivalence principle. *Bulletin of the American Physical Society* (2020).
51. Duan, W.-T. *et al.* Suppression of Coriolis error in weak equivalence principle test using 85 Rb-87 Rb dual-species atom interferometer. *Chinese Physics B* (2020).
52. Meng, Z., Yan, P., Li, X., Wu, K. & Feng, Y. *An Atom SAGNAC Interferometer With Continuous Cold Atomic Beam Sources* in *2020 IEEE International Symposium on Inertial Sensors and Systems (INERTIAL)* (2020), 1.

53. Moan, E. R. *et al.* Quantum Rotation Sensing with Dual Sagnac Interferometers in an Atom-Optical Waveguide. *Physical Review Letters* **124,** 120403 (2020).

54. Riley, K. F., Hobson, M. P. & Bence, S. J. *Mathematical methods for physics and engineering: a comprehensive guide* 3rd ed. (Cambridge university press, 2006).

Acknowledgements

A thesis work is a long and arduous journey, an endeavour that could not be done without the help of many others: mine, of course, was no exception.

I would like to firstly thank my supervisor, Dr. Francesco Minardi, for his constant support during this work, both from an academic and a human side, that ultimately made it possible for me to complete this thesis. Concurrently, I would also like to thank Dr. Chiara Fort and Dr. Alessia Burchianti, that helped me not only during my brief permanence in Florence, but also in the subsequent months. To all three: I would like to thank you for making me part of the team, and I will make sure that your trust in me was well placed.

I would also like to thank Dr. Marco Prevedelli, for the help during my first thesis month in Bologna and in general for introducing me to the world of atomic physics.

I would also like to thank my parents, that, since when I was a child, nurtured my curiosity and stimulated me, even when it meant pandering to an annoying kid. I am grateful for all you did for me, and without you I would not be who I am now.

Lastly, but not in importance, I would also like to thank all my friends, that have always been with me through the good times and the bad times.